

Characterization of peroxisomes and peroxisome deficient cell lines by super-resolution microscopy and biochemical methods

Doctoral Thesis

In partial fulfillment of the requirements for the degree “Doctor of Philosophy”

PhD in the Molecular Medicine Study Program

at the Georg-August University Göttingen



submitted by Kareem Salah Ahmed Mohamed Soliman

born in Alexandria, Egypt

Göttingen, 2016

Members of the Thesis Committee:

Supervisor Name, Institute: Prof. Jutta Gärtner, Department of Pediatrics and Adolescent Medicine, University Medical Center (UMG) Göttingen, Germany.

Second member of the thesis committee Name, Institute: Prof. Silvio Rizzoli, Department of Neuro- and Sensory Physiology, University Medical Center Göttingen.

Third member of the thesis committee Name, Institute: Prof. Stefan Jakobs, Max Planck Institute for Biophysical Chemistry Göttingen, Germany.

Date of Disputation: / / 2016

AFFIDAVIT

Here I declare that my doctoral thesis entitled “Characterization of peroxisomes and peroxisome deficient cell lines by super-resolution microscopy and biochemical methods” has been written independently with no other sources and aids than quoted.

Kareem Salah Soliman

Göttingen, June 2016

To my wife and family

List of publications:

1. **Kareem Soliman** “CellProfiler: Novel Automated Image Segmentation Procedure for Super-Resolution Microscopy” *Biological Procedure Online* 2015 17:11
2. Yifat Cohen, Yoel Alexander Klug, Lazar Dimitrov, Zohar Erez, Silvia G. Chuartzman, Dalia Elinger, Ido Yofe, **Kareem Soliman**, Jutta Gärtner, Sven Thoms, Randy Schekman, Yael Elbaz-Alon,* Einat Zalckvar* and Maya Schuldiner* “Peroxisomes are juxtaposed to strategic sites on mitochondria.” *Mol. BioSystems* RSC, 2014, **10**, 1742-1748.

Table of Contents:

List of tables	I
List of figures	II
Acknowledgments	III
Abbreviations	V
Abstract	VI
1. Introduction	1
1.1. Peroxisome biogenesis	1
1.2. Peroxisome proliferation and fission	4
1.3. Peroxisome Biogenesis Disorders (PBDs)	5
1.4. YGR168C regulates peroxisome abundance in yeast	6
1.5. Super-resolution STED microscopy	9
1.6. Automated Imaging analysis for super-resolution microscopy	11
1.7. Aim of this study	14
2. Materials and methods	15
2.1. Materials List	15
Chemicals list (A-Z)	15
Media and Buffers list	19
Equipment (A-Z)	31
Other materials (A-Z)	31
2.2. Methods	32
Preparation of Yeast competent cells	32
Yeast genomic integration	32
Yeast transformation.....	33
Nanobody staining and STED microscopy	33
Oleic acid growth assays	34
Amino acid intracellular metabolomics.....	35
DNA cloning and plasmids.....	35
Patient-derived skin fibroblast.....	35
Cell culture, transfection and immunofluorescence	36
Nanoboosted GFP and RFP in HeLa cells	37
Widefield microscopy.....	37

STED microscopy setups	37
Subdiffraction size analysis.....	38
CellProfiler: automated STED analysis.....	38
<i>CellProfiler</i> : ghost peroxisomes quantification	39
Protein extraction by non-ionic detergents.....	40
Blot imaging and data analysis	41
GFP-trap co-immunoprecipitations experiments.....	42
3. Results.....	43
3.1. Characterization of PEX35: a novel regulator of peroxisome abundance.....	43
Super-resolution microscopy demonstrates opposing effects for loss or overexpression of YGR168C	43
YGR168C is a new <i>PEX</i> gene (<i>PEX35</i>).....	45
Characterizing the molecular function of PEX35.....	47
3.2. Characterization of human peroxisomes	49
Peroxisome subdiffraction structure in normal and proliferating condition ...	49
DLP1 and MFF localization on peroxisomes at the nanoscale	53
Super-resolution STED analysis of ZS ghosts	59
STED resolution is essential for accurate ghost size analysis	63
Ghost size in ZSS patients correlates with total PMP70 protein abundance	64
Peroxisome abundance does not correlate with PMP70 abundance.....	65
PEX2 interacts with PMP70 <i>in vivo</i>	66
4. Discussion.....	69
4.1. PEX35 a regulator of peroxisome abundance.....	70
4.2. Mammalian peroxisomal translocon proteins localizations	72
4.3. ZSS ghost phenotype characterization	73
5. Conclusion	75
6. Appendix	76
6.1. Matlab Script codes.....	76
7. Bibliography.....	79
Curriculum Vitae	95

List of tables

Table 2-1 Yeast Growth Media	19
Table 2-2 Yeast Competent cells and transformation buffer	21
Table 2-3 Genomic DNA isolation buffers.....	22
Table 2-4 Antibody immunofluorescence reagents.....	23
Table 2-5 Nanobody staining reagents	24
Table 2-6 Western blot and co-immunoprecipitation (CoIP) solutions and buffers	25
Table 2-7 Antibodies list.....	29
Table 3-1 Patients Summary	62

List of figures

Figure 1.1 Confocal microscopy of peroxisomes.	2
Figure 1.2 Peroxisome biogenesis model.	3
Figure 1.3 STED microscopy, principle.	10
Figure 1.4 Fluorescent gold beads STED microscopy resolution.	13
Figure 3.1 STED subdiffraction size and phenotype analysis of yeast peroxisome in Pex35 mutant strains.	44
Figure 3.2 YGR168C is a new peroxin (PEX35).	46
Figure 3.3. Intracellular amino acid metabolome analysis.	48
Figure 3.4 STED nanoscopy reveal peroxisome membrane and lumen.	50
Figure 3.5 Two-color STED nanoscopy of peroxisome membrane and matrix. ...	51
Figure 3.6 STED subdiffraction imaging of hyper-tubulated peroxisomes.	52
Figure 3.7 Mitochondrial wtDLP1 ring structures on mitochondrial constricted and invaginated membranes (arrow).	54
Figure 3.8 STED nanoscopy of DLP1 and MFF at peroxisomal constriction sites.	55
Figure 3.9 Peroxisomal localization of fluorescently labeled PEX proteins	57
Figure 3.10 STED visualization of fluorescently tagged Docking and RING peroxins reveal distinct localization of each subcomplex on adjacent membranes.	58
Figure 3.11 ZS ghost peroxisomal remnants STED analysis.	60
Figure 3.12 Diffraction-limit Gaussian blur and ghost size analysis.	63
Figure 3.13 PMP70 protein level in ZS patients correlates with ghost size STED phenotype.	65
Figure 3.14 Peroxisome ghost quantification.	66
Figure 3.15 PEX2-PMP70 interaction in vivo.	68

Acknowledgments

First and foremost, I would like to thank my principal supervisor Prof. Jutta Gärtner for giving me this great chance to work in her pioneering group, which includes great medical staff and researchers. I appreciate all her time, ideas, and funding to make my PhD experience great and stimulating. I wish to express my sincere appreciation and gratitude to my co-supervisor PD. Dr. Sven Thoms for his continuous encouragement and for giving me the chance to work with him on very exciting projects and ideas.

The members of Prof. Hell's Group with special thanks that goes to Dr. Fabian Göttfert, Prof. Stefan Hell, and Dr. Dirk Kamin. They facilitated the STED microscopy throughout my PhD time. In addition, Dr. Göttfert was very helpful and provided me with STED images for my method paper. Prof. Hell has also been very supportive to me and my project. It was an honor to do the imaging part in his lab at the Max Planck Institute of Biophysical Chemistry.

The PhD project is not a singlehandedly work, therefore, I have to thank Elisabeth Ehbrecht and Corina Dickel for their technical assistance. I was lucky to work in a lab that has its own DNA sequencing facility, which is managed and operated by Dr. Andreas Ohlenbusch. I would like also to thank Dr. Hendrick Rosewich for providing me with patients' data. I wish also to thank Dr. Ralph Krätzner and Monika Schneider, without their help, the amino acid metabolome analysis would not have been possible. There are a lot of people in my lab whom I would like to thank and express my sincere appreciation, but I can't describe how great they are and their support was a very important part of my success "Thank you".

I have had the chance to supervise and meet wonderful young people: Judith Büntzel, Christopher Nötzel and Uta Bickmeyer. I really enjoyed working with them and supervising some of them on very interesting projects and ideas. Their young energy was always an encouragement. We worked together on very interesting ideas; some of the ideas worked and others led to fruitful conclusions.

Acknowledgments

Special thanks to Uta Bickmeyer for her feedback after reading the multiple versions of my thesis discussion. I also would like to thank Dr. Thomas Weber for reading the final draft of my thesis and for giving me valuable comments and feedbacks. To my colleague and friend Dr. Rosemol George: we started our PhD together at the same time in the same lab. I am happy that she made it and successfully received her Doctoral degree.

The group of Dr. Maya Schuldiner's lab, I would like to thank them on the great collaborative experience. I also would like to thank Dr. Cindy Krause for providing me with DNA plasmids.

Without the financial funding from the German Research Foundation (DfG) and the Open Access Publication Funds of Göttingen University, this work would not have been possible.

Special thanks to my thesis committee members: Prof. Silvio Rizzoli and Prof. Stefan Jakobs. Their feedbacks and advices surely contributed to the final success of my work. Unfortunately, we lost Prof. Uwe-Karsten Hanisch during my PhD work (May his soul rest in peace). He was one of the members of my PhD advisors' committee and he contributed to the development of my PhD work at the beginning of my PhD.

Last but not least, I would like to thank my amazing support team "my wife Magda and my son Moustafa" for their love, support, and encouragement. They have gone through this journey with me. My parents (my mother and my father), without your unconditioned love and support I would not have been the person standing in front of you today. My family does not stand here, it includes my wife's parents, who are to me a mother and a father too. I wish to say all the names here: Amira and her family (sister), Ahmed and his family (brother), Emaan (sister in law), Mohamed (brother-in law), Omar (brother-in law), and Ali (brother-in law).

Kareem S. Soliman

Abbreviations

ACAA1 Acetyl-Coenzyme A acyltransferase 1

Arf ADP-ribosylation factors

CAT1 Catalase enzyme

EM Electron microscopy

ER Endoplasmic Reticulum

FWHM Full-Width-Half-Maxima

HSF Human Skin Fibroblast

mPTS Membrane Peroxisomal Targeting Signal

PALM Photoactivatable Light Microscopy

PBD Peroxisomal Biogenesis Disorder

PMP Peroxisomal Membrane Protein

PTS1 Peroxisomal Targeting Signal – 1

PTS2 Peroxisomal Targeting Signal – 2

STED Stimulated Transmission Emission Depletion microscopy

STORM Stochastic Reconstruction Microscopy

ZS Zellweger Syndrome

ZSS Zellweger Syndrome Spectrum

Abstract

Stimulated Transmission Emission Depletion (STED) microscopy was used to characterize the nanoscopic morphology of wild-type peroxisomes under normal and proliferative conditions in mammalian cells and in yeast *Saccharomyces cerevisiae* (in this text referred to as yeast). In yeast, the new peroxisomal protein Pex35 was characterized by analyzing the subdiffraction size and morphology of peroxisomes in wildtype, and *pex35* mutant strains. Only STED microscopy could reveal the Pex35 overexpression phenotype, which resembled hyper-vesiculation of clumped peroxisomes within a subdiffraction volume. This remarkable subdiffraction phenotype supports the hypothesis that PEX35 regulates peroxisome abundance by an Arf1 dependent vesiculation mechanism.

In mammalian HeLa cells, the colocalization of the translocon complex and peroxisomal fission factors on peroxisome membranes were analyzed at the nanoscale. RING (PEX2-PEX10-PEX12) and docking (PEX13-PEX14) subcomplexes of the translocon machinery were found to localize on distinct membrane substructures. We also used STED microscopy, and developed an automated imaging analysis pipeline in *CellProfiler* (www.cellprofiler.org) to analyze the sub-diffraction morphology of the cellular peroxisomal ghost phenotype in Peroxisome biogenesis disorder patient cells (Zellweger Syndrome Spectrum phenotype). The size of the peroxisomal ghosts was found to correlate with import deficiency, integral peroxisomal membrane (PMP70) protein abundance, and the clinical severity of the patients. This is the first time that the membrane ghost phenotype associated with Zellweger Syndrome Spectrum disorder could be shown to correlate with the clinical severity and import deficiency in patients' fibroblasts. Overall, this work forwards the characterization of the peroxisome organelle in wildtype conditions and human peroxisomal disorders.

1. Introduction

1.1. Peroxisome biogenesis

Peroxisomes are single membrane bound eukaryotic organelles that carry important metabolic and signaling functions. They were first described using electron microscopy (EM) in liver tissues, and in 1966, Christian De Duve described a microsomal liver fraction that was rich in catalase, a hydrogen peroxide detoxifying enzyme, and hence they were termed “peroxisomes” [1]. Peroxisomes are evolutionary conserved in many species, except for some eukaryotes which do not have peroxisomes, others may contain specialized classes of peroxisomes that have different designations [2]. For example, in *Neurospora crassa*, fungi they are known as “woronin bodies” and *Trypanosoma brucei* parasites they are named “glycosomes” [3, 4]. In humans, peroxisomes are ubiquitous in all cells, except for mature red blood cells [2]. The ultrastructure of peroxisomes has been extensively studied using EM methods: Peroxisomes have normally spherical structures, but they can also have tubular, elongated structures that show segmentation [5]. In general, their size can vary between 50 nm and 1 μm [2]; however, in mammalian cells, the majority of peroxisomes shows a small profile (50 – 200 nm in diameter) [5], which lies at the diffraction limit of light microscopy [6].

Peroxisomes are semiautonomous organelles, they derive their membranes from endoplasmic reticulum, but they can also form by division from pre-existing peroxisomes [7]. Peroxisome lumen (matrix) is filled with matrix proteins most of which are metabolic enzymes [2]. Matrix proteins are imported into peroxisomes using peroxisomal targeting sequences: PTS1 (C-terminus) or PTS2 (N-terminus) via PEX5 and PEX7 soluble matrix receptors, respectively [8]. Matrix proteins have been shown to translocate into peroxisomes in their oligomeric folded form and it is thought that the translocation mechanism does not require energy (ATP), but recycling of matrix receptors back to the cytosol is energy dependent [9, 10]. Diffraction-limited fluorescence microscopy reveals

peroxisome matrix and membrane proteins as perfectly colocalized structures and it is not possible to demarcate the peroxisomal compartment with the peroxisomal membrane (Fig. 1.1).

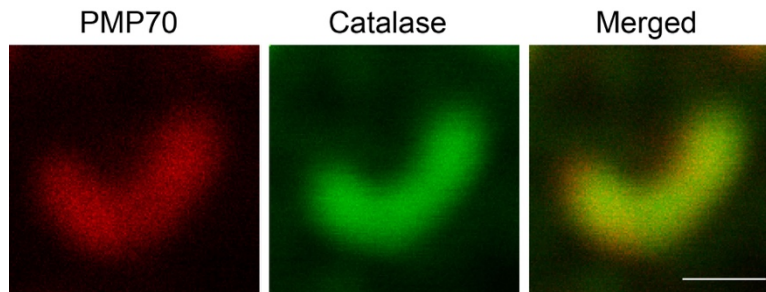


Figure 1.1 Confocal microscopy of peroxisomes.

Single peroxisome in Human Skin fibroblast (HSF) cell stained with PMP70 (left) and Catalase (middle) primary antibodies. Labeled with KK114 and Atto590 conjugated secondary antibodies, respectively. Merged overlay (right). Images were smoothed with 3x3 average filter. Scale bar 500nm.

The process of peroxisome biogenesis (*de novo* synthesis) can be divided into two events: 1) early membrane biogenesis, and 2) translocon maturation and matrix protein import, both of which require PEX gene-encoded peroxins [11]. Most peroxins are integral peroxisomal membrane proteins (PMPs), while some are soluble proteins that show bimodal distribution between the cytosol and peroxisomal membranes, e.g. PEX5, PEX1 and PEX6 (AAA proteins) [12]. They are named and numbered by order of identification (e.g. PEX1, PEX2, etc.) [13]. In the yeast *Saccharomyces cerevisiae*, which I will refer to as yeast throughout the text, there are 34 peroxins, whereas in humans there are only 14 known peroxins [2]. A current model of peroxisomal membrane biogenesis implies that type-III membrane peroxins, also known as early membrane peroxins (PEX3, PEX16 in humans, and PEX27 in yeast), which target to the ER, primarily with help of the ER secretory apparatus [14, 15]. Early membrane peroxins together with PEX19, a soluble cytosolic chaperone, are then required for the direct targeting of type-I integral PMPs from the cytosol to peroxisomal sites at the ER

[16]. Integral PMPs contain a membrane peroxisomal targeting sequence (mPTS) [17]. Type-I integral PMPs are the RING subcomplex peroxins (PEX2, PEX10, and PEX12) and the docking subcomplex components (PEX13 and PEX14) of the peroxisomal translocon, in addition to membrane transporters, e.g. PMP70 and ALDP [18]. Type-I integral PMPs are translated on free cytosolic polysomes, despite the fact that some of them have been shown to carry ER targeting signals, e.g. PMP70 [19].

In yeast, it has been shown that RING and docking components localize to distinct ER derived pre-peroxisomal vesicles, which later mature into import competent peroxisomes via heterotypic fusion aided by PEX1 and PEX6 AAA membrane associated peroxins (Fig. 1.2) [20].

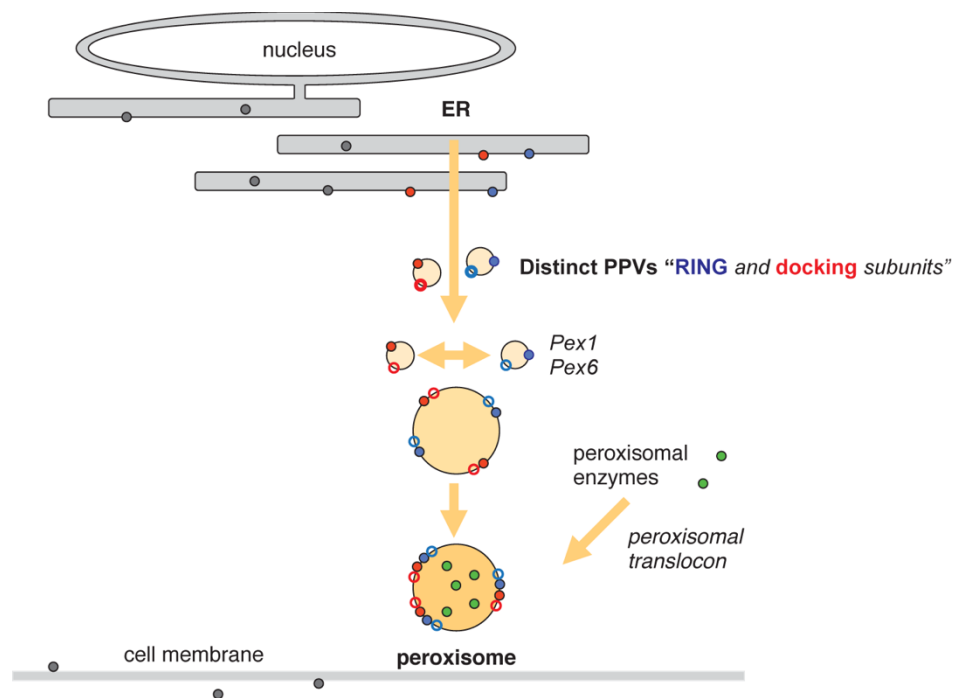


Figure 1.2 Peroxisome biogenesis model.

Two pre-peroxisomal vesicles (PPVs) arise from the ER harboring RING and docking subunits, which fuse by help of PEX1 and PEX6. The resulting mature translocon translocates matrix proteins into the peroxisomal matrix. (Adapted from Van der Zand, et al. 2012).

When a mature peroxisomal translocon is formed, cargo matrix receptors dock and translocation of cargo to the inner peroxisomal membrane matrix space occurs [21, 22]. However, in mammals how the translocon is formed is not clear and the colocalization and distribution of RING and docking peroxins remains to be elucidated.

1.2. Peroxisome proliferation and fission

In addition to *de novo* synthesis, peroxisomes control their abundance by proliferation and division using PEX11 proteins [23], and fission factors that are shared with mitochondria [23]. The transcriptional regulation of peroxisome proliferation is carried out by the Peroxisome Proliferator-Activating Receptors (PPARs), and Oleate activated factors (Oafs) in humans and yeast, respectively [24, 25]. There are pharmacological substances, hypolipidemic drugs, that can stimulate peroxisome proliferation and hence increase their abundance [26, 27]. Further, yeast grown on glucose-rich media, contains fewer (2-3 per cell) and smaller peroxisomes (100 – 200 nm), [12]. Since beta-oxidation of very long chain fatty acids (VLCFAs) is a key metabolic pathway that only takes place in peroxisomes, it was shown that by adding VLCFAs, such as Oleic acid or Palmitic acid to yeast cultures, peroxisome proliferation and division is induced [28]. Such chemicals have been used to assess peroxisome function and aided the discovery of new peroxisomal proteins [29].

Induced peroxisomes require PEX11 protein for elongation and fission [30]. In humans, there are three of PEX11 isoforms (alpha, beta, and gamma), with PEX11beta being the most important one responsible for majority of peroxisomal proliferation events in the cell [31]. Overexpression of PEX11beta leads to elongated peroxisome (hypertubulation) [31, 32]. The ultrastructure of these hypertubulated structures indicated a steady subdiffraction diameter of 80 – 100 nm [31]. PEX11 has been shown to accumulate at constriction sites with other fission factors like Dynamin-Like-Protein-1 (DLP1), and is thought to

contribute to fission by a membrane deformation mechanism [33]. DLP1 (or Dnm1 in yeast), a small GTPase proteins that forms helical rings around mitochondrial and ER membranes to induce constriction and fission, was the first peroxisomal fission factor discovered [34]. PEX11 overexpression recruits DLP1 to peroxisomes, and other fission proteins were shown to be important for the recruitment of DLP1 to peroxisome membranes [23, 35]. For example, the tail-anchored Mitochondrial Fission Factor (MFF) and Fission factor 1 (FIS1) proteins [36]. Using indirect immunofluorescence and conventional fluorescence light microscopy DLP1 was found to localize on peroxisomal membrane termini in PEX11 overexpression [34]; however, the function of DLP1 at termini is unknown. Unlike for mitochondrial DLP1 [37], there are no quantitative data about peroxisomal DLP1.

1.3. Peroxisome Biogenesis Disorders (PBDs)

Mutations affecting *PEX* genes are the cause of rare lethal metabolic disorders, termed as Peroxisome Biogenesis Disorders (PBD) [38]. PBDs are neurological pediatric disorders that lead to early lethality in the majority of the cases. PBDs can be divided into two groups: (1) Zellweger Spectrum Syndrome (ZSS) affecting up to 16 *PEX* genes (i.e. 16 complementation groups), and (2) Rhizomelic Chondrodysplasia Punctata Type-1 (RCDP-1) where only *PEX7* is involved [39]. RCDP-1 mutations lead to import defects of PTS2 matrix proteins, while ZSS mutations cause PTS1 and PTS2 import defects, with mutations in *PEX1* being responsible for ~ 80% of the cases [40, 41]. The ZSS is a continuum of clinical symptoms with the most severe and mildest cases, the Zellweger syndrome (ZS) and Heimler Syndrome (HS), respectively [39, 42]. ZS patients show a genotype-phenotype correlation, which means that the severity of the phenotype correlates with the severity of mutation on the function of the encoded protein [41]. Low abundant membrane remnants (ghosts) structures devoid from matrix content, and accumulation of VLCFA are cellular hallmarks of ZS [41]. Ghosts ultrastructure in EM appear as enlarged membrane structures with heterogeneous size and morphological distribution with positive membrane

protein content [43]. There are no quantitative data and phenotype-genotype correlations with respect to ghost structures in ZS. In human cells, it is very difficult to find them by EM; however, early EM data have revealed ghost structures that can reach two to four times the size of normal peroxisome [44]. Immunofluorescence imaging provided a good alternative method to visualize human ghost structures and patterns [44]. Using manual scoring and wide-field microscopy, ZS patients' skin fibroblast cells with higher frequency of large ghosts have been found, while other patients' cells revealed normal size peroxisome structures or a mixed pattern of both large and normal size ghost particles [44]. After the identification of affected genes in humans and yeast, data suggest that enlarged abnormal ghosts' particles indicate mutations in AAA peroxins (PEX1 and PEX6) and docking factors (PEX13 and PEX14), whereas mutations in RING peroxins are accompanied by virtually normal ghost appearance compared to control cells [44, 45]. Mutations affecting early membrane peroxins and PEX19, were shown to be devoid of membrane remnants leaving integral PMPs unstable [46]. Despite the early efforts to classify ghosts in ZS patients' cells, a proper quantitative classification does not exist, and in humans PEX10 and PEX13 ghosts' pattern remains to be elucidated. Further, differences in protein levels of the integral PMP, PMP70, have been observed in biopsies of different ZS patients [47]; however, whether differences in protein abundance play a role in the ghost size heterogeneity in these patients remains unknown.

1.4. YGR168C regulates peroxisome abundance in yeast

Yeast is one of the well characterized and most frequently used models to study organelles and their biogenesis, including peroxisome [48]. Most *PEX* genes in humans are evolutionary conserved in yeast and many orthologues were first identified in yeast [2]. Easy genetics, faster doubling time, and ease of handling favored yeast systems over mammalian systems in the discovery of new peroxisomal proteins [49]. Yeast cells can be maintained in their haploid or diploid states, which offers the advantage of direct observation of knockouts in

the haploid state, while the diploid state can be used for crosses to produce haploid strains, for example, with multiple knockouts [50]. As mentioned earlier, there are 34 *PEX* genes in yeasts; PEX34 is the last identified peroxin, which functions together with PEX11 to control peroxisome numbers [51]. PEX11 family proteins in yeast consist of Pex11, Pex25 and Pex27, which are involved in peroxisome fission and proliferation [2]. Other proteins, which target to different organelles and locations in the cell e.g. DLP-like Vps1, actin, myosin receptor (Myo2p) and ADP-ribosylation factors (Arfs), have been also shown to control peroxisome abundance and inheritance [52, 53]. Despite the large number of factors discovered that control peroxisome numbers, the mechanism by which peroxisome abundance is controlled remains elusive. This maybe partially due to unknown key players in the mechanism controlling peroxisome abundance that remain to be elucidated.

Initially, yeast screens were dependent on growth on oleic acid plates to identify *PEX* genes due to their ability to utilize oleic acid (C18:1), which can only be metabolized by peroxisomes [54, 55]. Yeast strains with defects in peroxisome abundance or beta fatty acid oxidation function show reduced halos around colonies, and reduced growth in oleic acid liquid cultures as well as reduction in oleic acid consumption [56, 57].

Microscopic screening methods have recently gained increased interest, because they offer additional readouts compared to metabolic growth effects [58, 59]. Improved genetic integration cassettes, deletion and overexpression libraries collections, and synthetic genetic array (SGA) genetic interaction analysis in combination with HTS assays provided new results [59, 60].

Our lab in collaboration with M. Schuldiner's Lab has initiated a genome wide-screen to hunt for more peroxisomal proteins that control peroxisome abundance or size. To achieve that, our lab first constructed a query strain with fluorescently tagged early membrane peroxin (PEX3-mcherry) and ER marker protein (Spf1-GFP), then they performed automated SGA crossings of this query strain into a yeast deletion library of ~ 4600 non-essential genes and ~ 1800

essential genes, as described earlier [61]. Using HTS microscopy and high-content screening they analyzed peroxisome number per cell, and they found enriched *PEX* genes and other peroxisome associated proteins known to affect peroxisome number on top of their list. Among the top list of proteins, a previously uncharacterized gene, *YGR168c*, appeared with severe reduction in peroxisome number. Colocalization widefield microscopy analysis revealed peroxisomal colocalization of its encoded protein. Interestingly, deletion and overexpression of *Ygr168c* showed reduction in peroxisome abundance under glucose as well as oleic acid conditions (Yofe et al, unpublished).

Multiple screens were then carried out to characterize the function of *Ygr168c*. First, a synthetic lethality screen has been done to uncover important pathways when *ygr168c* is mutated, in which a *ygr168c* deletion strain was crossed with a deletion library comprised of ~ 6000 genes, previously used in the microscopy screen (Yofe et al, unpublished). The synthetic lethality screen demonstrated a strong link between *YGR168C* with genes of redox homeostasis and amino acid metabolism e.g. arginine biosynthesis. Another protein-protein interaction screen that used fragment complementation of two parts of dihydrofolate reductase (DHFR) was carried out to attempt further characterization of *YGR168C* function with respect to number and size of peroxisomes. The interaction split assay enabled the tracking of *YGR168C* interaction with all yeast proteins (Yofe et al, unpublished). The results of DHFR interaction screen indicated several *PEX* and non-*PEX* interaction partners to *YGR168C*, which play roles in peroxisome biogenesis and division. Most importantly, the *PEX11* family proteins: *PEX11* and *PEX25*, and the *ARF* proteins: *Arf1* and *Arf2* (Yofe et al, unpublished). Further, *YGR168c* overexpression was shown to lead to *Arf1* dissipation from the Golgi to the cytosol, which is reminiscent of increased GTPase Activating Protein (GAP) activity or decrease in Guanine nucleotide Exchange Factor (GEF) activity (Yofe et al, unpublished). Deletion of *Arf1* in $\Delta ygr168c$ lead to worsening of the $\Delta ygr168c$ phenotype, while deletion of *Arf1* in *YGR168C* overexpression strain

rescued peroxisome size and numbers (Yofe et al, unpublished). Why peroxisomes appear bigger and less in both of ygr168c deletion and overexpression in confocal microscopy remains puzzling and require further investigation.

1.5. Super-resolution STED microscopy

Diffraction-limited light microscopy cannot resolve structures at a distance below 200 nm, because light propagates as a wave and thus constrained by a physical phenomenon known as “diffraction” [62]. The diffraction limit is about $\frac{1}{2}$ the wavelength of excitation light (visible light spectrum: 400 nm – 800 nm), as described in the 19th century by Ernst Abbe’s equation [63]. In the 21th century, the diffraction barrier was broken in experiments conducted by Stefan Hell, William Moerner, and Eric Betzig [64]. Previous ideas to improve resolution were focused on improving optical elements of microscopy and imaging near to specimen (near-field microscopy), which was impractical for many cell biology applications compared to far-field microscopy [63]. The basic principle of Stefan Hell, Eric Betzig, and William Moerner ideas and experiments was to modulate the transition state of fluorescence molecules rather than improving optics, and this laid the foundation of far-field super-resolution microscopy [65]. According to their work, the ON/OFF (excited “fluorescence” and de-excited “dark”) states of fluorophores can be modulated temporally or spatially by stochastic emission and stimulated emission, respectively [66, 67]. Photoactivatable Light Microscopy (PALM) and Stochastic reconstruction microscopy (STORM) use temporal properties to obtain super-resolution images; they depend on the photo activation of photo switchable fluorophores or the stochastic activation of fluorescent molecules by using short excitation pulses, respectively, and images are collected by camera grid over many cycles of frames [68]. In each frame, only a subpopulation of single fluorophore emitters is turned ON, and at the end of repetitive light activation, a super-resolution image is reconstructed mathematically by defining the center of mass of single emitters and their

position on the camera detector [69]. In the case of Stimulated Transmission Emission Depletion (STED) microscopy, two co-aligned laser beams are used; one excitation beam and another azimuthally polarized (doughnut -shaped) depletion (STED) beam with a zero minima intensity ($I_{STED} \approx 0 \text{ mW}$) at the doughnut center [70]. When the two beams illuminate a fluorescent sample, only the molecules from the center of the doughnut are excited, whereas the other molecules hit by the STED beam are de-excited instantaneously to the reversible non-fluorescent (dark) states [66, 71]. Using the same principle of diffraction, the doughnut's center can be adjusted, to few nanometers, by increasing the power of the depletion beam (Fig1.3) [71, 72].

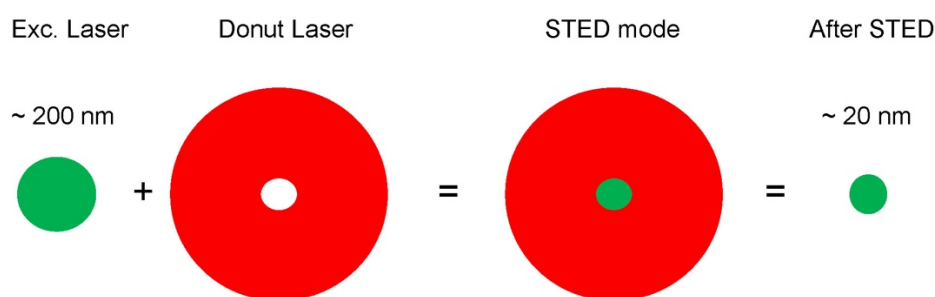


Figure 1.3 STED microscopy, principle.

Cartoon illustrating the principle of Stimulated Transmission Emission Depletion (STED) microscopy and resolution enhancement provided by STED laser. The green circle indicates the excitation laser focus and the red doughnut circle indicates the STED laser.

In practice, STED microscopes reach a resolution of 20 - 30 nm because of depletion efficiency at lower STED power and the irreversible chemical destruction of organic fluorescent molecules (photobleaching) at high laser powers [73]. Gated-STED, pulsed-STED lasers, or a combination of the two techniques enabled efficient STED imaging at high resolution within acceptable laser powers for both live and fixed biological samples [74]. Using very stable fluorophores, e.g. nanodiamond crystals, it is possible to increase lasers to very

high powers and achieve a resolution down to the dimensions of atoms (0.1 nm) [75, 76]; however, stable organic fluorophores remain the best choice when it comes to life sciences applications. Two excitation laser (two color) STED microscopy with one depletion beam has been successfully shown to obtain two color super-resolution images using two spectrally distinguishable dyes, with resolution down to 20 nm in X-axis and Y-axis in both recorded channels [77]. This offered great advantage to conventional confocal colocalization microscopy, because only excited fluorophores from the center of the STED doughnut emit fluorescence in both wavelengths, which means that there will be no offset error that normally occurs due to the need to align the excitation lasers [77].

Super-resolution microscopy offers a useful tool in biology, because most of biological structures revealed a size and ultrastructure below diffraction limit of light [68]. The first super-resolution images in a cell showed vacuolar membrane details in yeast at unprecedented details [78]. Many eukaryotic organelles have been revealed at nanometer resolution using super-resolution microscopy [79–82]. Antibody immunofluorescence has been the most used technique, to label biological samples for super-resolution imaging, because it offers high labeling densities and photostability of the conjugated organic fluorophore dyes [83]. Although antibody labeling remains the most commonly used labeling strategy, they impose disadvantages that become evident at subdiffraction resolution, such as big label size and the steric hindrance [84]. Therefore, smaller affinity labels such as single-domain antibodies (nanobodies) or small-nucleic-acid ligands (aptamers), were developed and effectively used to overcome such complications that may associate conventional antibodies [85–88].

1.6. Automated Imaging analysis for super-resolution microscopy

Image analysis of images obtained from fluorescence light microscopy can be a very subjective task if performed manually, which may introduce bias to final

results. Therefore, automated analysis pipelines offer an alternative to approach this problem [89]. Automated imaging analysis tools for fluorescence imaging have been developed, because of their importance for high-content-screening (HCS) and HTS cellular assays [90]. However, automated freeware analysis tools for super-resolution microscopy are not widely available and may still require further development to bring it to full automation [91–93]. When structures are revealed by super-resolution microscopy, it is often the case that structures reveal a subdiffraction pattern or clusters of biomolecular complexes and proteins. For instance, a nuclear pore immunostained with an outer ring marker, the scaffold protein gp210, revealed each nuclear composed of an average of ~ 8 gp210 subunits when imaged using STORM or STED microscopy [91]. So far, segmentation and analysis of individual nuclear pores for quantitative purposes, was accurately achieved by active cropping of individual pores or template matching algorithms, which is a very time consuming and requires Matlab (www.mathworks.com) programming skills, respectively [91]. Therefore, developing a method in which computer algorithms can automatically segment individual nuclear pores, at the same time exempting the user from prior knowledge or cost of any programming language will be substantially beneficial. Recently, an automated algorithm has been described that uses adaptive local density estimation kernels, in order to merge or separate groups of subdiffraction structures based on local density information [94]. However, such an algorithm is not yet available in readily available user-friendly platforms, and has only been tested on images from biological structures with continuous density profiles, such as mitochondria and tubulin. Developing another method that can be immediately implemented, and is able to efficiently segment structures with irregular fluorescent patterns and densities in images obtained by super-resolution microscopy, will be of great advantage.

Super-resolution microscopy techniques provide a much narrower Gaussian point spread function (PSF) of the focused scanning area, enabling us to resolve features that are distant below the diffraction limit of light [68].

Smoothing functions algorithms are generally applied to images and to single-molecule localization (image coordinate) data, in order to enhance structure/cluster segmentation [95]. Applying a Gaussian filter could also enlarge PSF of super-resolution images and drive resolution backward toward the diffraction limit of light in a controlled fashion by mathematical means e.g., increasing width of Gaussian (Fig 1.4).

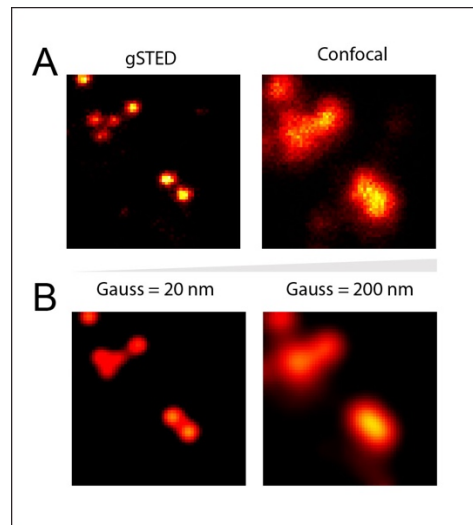


Figure 1.4 Fluorescent gold beads STED microscopy resolution.

(A) Raw STED image of 80 nm fluorescent gold beads (left) and Confocal overview (right) (B) Gaussian smooth of STED image image with sigma = 20 nm (left) and Gaussian smooth with sigma = 200 nm (right).

An intuitive way to segment SR images (subdiffraction patterns) into meaningful objects would be through Gaussian smoothing to merge proximate signals within the artifact radius of the Gaussian. Once this grouping is achieved, fused neighboring objects remain to be segmented. Merged super-resolved subdiffraction structures might show intensity variation throughout the whole object. For that, it is logical to use algorithms that use shape information to segment clumped objects, avoiding by that over-segmentation problems [96]. Once objects in an image are perceived as biologically significant objects by means of Gaussian blurring and optimized imaging segmentation, it should

remain possible to segment the actual SR image to find out single molecule clusters or subdiffraction pattern information within objects. Associating objects found in the SR image and its Gaussian blur, would then allow us to find out meaningful data about the biological structures in question. Free imaging software tools like CellProfiler (www.cellprofiler.org), possess all previously described algorithms and analysis paradigms [97], which should make it possible to implement Gaussian blur filters and combine image segmentation procedures to extract meaningful data from SR images in a fully automated way.

In this thesis, an automated imaging analysis method has been developed, based on Gaussian [98], which will be later used to analyze peroxisome structures (ghosts) in ZS patients.

1.7. Aim of this study

The aim of this work: 1) Characterize a novel peroxisomal yeast protein, mainly by using STED super-resolution microscopy, in addition to intracellular HPLC-amino acid metabolomics, and biochemical techniques. 2) Study the subdiffraction morphology of peroxisomes in humans as well as the peroxisomal protein arrangements in wild-type and ZSS patient fibroblasts by STED microscopy and biochemical techniques.

2. Materials and methods

2.1. Materials List

Chemicals list (A-Z)

A

Acetone $\geq 99,7\%$, Ph. Eur (Art Nr. CP40.2, ROTH)

Agar-Agar Kobel (Art Nr. 5210.2, ROTH)

Agarose Molecular Biology grade (Art Nr. 4105, Biochemica)

Albumin Fraction V $\geq 98\%$, powdered for molecular biology (Art Nr. 8076.2, ROTH)

Amino acids (all from Sigma and ROTH)

Ammonium Sulfate $\geq 99\%$, for molecular biology (Art Nr. A4418-1KG, Sigma)

B

BC Assay Reagent A (UP95424A, Uptima)

BC Assay Reagent B (UP95425, Uptima)

BigDye Terminator v.1.1 v.3.1 5x sequencing buffer (Applied Biosystems)

Bromophenol Blue (Merck)

C

Complete Easypack cocktail protease inhibitor (Art Nr. 04693116001, Roche)

Concanavalin A (ConA) from *Canavalia ensiformis* (Jack bean) Type IV, lyophilized powder (Art Nr. C2010-25MG, Sigma)

D

D (+) Glucose nonhydrous (Art Nr. X997.2, ROTH)

Dithiothreitol (DTT) (Art Nr. 20710.04, SERVA)

Dulbecco's MEM (DMEM) – Low (1g/L D-Glucose) (Art Nr. F0415, Biochrom)

E

EDTA solution pH 8.0 (0.5 M) for molecular biology (Art Nr. A4892.0500, AppliChem)

Ethanol absolute for analysis EMSURE® ACS, ISO, Reag. Ph. Eur (Art Nr. 1.00983.2500, MERCK MILLIPORE)

F

Fetal Bovine Serum (FBS) Superior standardized (Art Nr. 90615, Merck)

G

Glycerol 99% (Art Nr. G901-2, Sigma)

Glycine PUFFERAN® ≥99 %, p.a. (Art. 3908.2, ROTH)

L

LB-Agar (Art Nr. X969.1, ROTH)

Lithium Acetate dihydride (L4158-250G, Sigma)

M

Methanol, 'BAKER ANALYZED' (Art Nr. 8045.2500, AVANTOR)

Milk Buffer, Blotting grade (Art Nr. T145.3, ROTH)

N

Nonidet™ P-40 (NP-40) (Art Nr. 74385-1L, Sigma)

O

Oleic acid ≥99% (GC), stored in the dark at -20°C (Art Nr. O1008-5G, Sigma)

P

Paraformaldehyde 37% (Art Nr. 1.04003.1000, Merck)

PBS Dulbecco w/o Ca²⁺ w/o Mg²⁺ low endotoxin (Biochrom)

Penicillin-Streptomycin antibiotics (Art Nr. A2213, Merck)

Peptone ex casein tryptic digest, for microbiology (Art Nr. 8986.2, ROTH)

Phenylmethanesulfonyl Fluoride (PMSF) (Art Nr. A0999.0029, AppliChem)

Polyethylene Glycol (PEG) 4000 (Art Nr. 0156.1, ROTH)

Ponceau S solution Ponceau S solution BioReagent, 0.1 % (w/v) in 5% acetic acid (Art Nr. P7170-1L, Sigma)

Potassium Chloride ≥99, 5 %, p.a., ACS, ISO (Art Nr. 6781.1, ROTH)

Potassium dihydrogen phosphate ≥99 %, p.a., ACS (Art Nr. 3904.1, ROTH)

Potassium phosphate dibasic trihydrate (Art Nr. 16788-57-1, Sigma)

S

Sodium Chloride (Art Nr. 3957.1, ROTH)

Sodium dodecyl sulfate, 10% (10%-SDS) (Art Nr. 155553-035, Gibco)

Sodium dodecyl sulfate, 20% (20%-SDS) (Art Nr. 1057.1, ROTH)

Sodium hydroxide (Art Nr. 1.06459.1000, Merck)

Sorbitol (Art Nr. 6213.2, ROTH)

Stempro-Accutase, cell dissociation reagent (Art Nr. A11105-0, Gibco)

T

TEMED GE health care (Art Nr. GE17-1312-01, Sigma)

Trichloroacetic acid (TCA) (Art Nr. 91228-500G, Sigma)

TRIS PUFFERAN® ≥99, 9 %, Ultra Qualität (Art Nr. 5429.3, ROTH)

Triton-X-100 (Art Nr. 3051.2, ROTH)

Trypan Blue 0.5% (w/v) in PBS (Art Nr. L6323, Biochrom Ac)

Trypsin EDTA 1x (Art Nr. 594170-100ML, Sigma)

Tween 20% (Art Nr. S413784432, Merck)

Tween 40% (Art Nr. P1504 – 500ML, Sigma)

Y

Yeast Extract powdered, for bacteriology (Art Nr. 2363.5, ROTH)

Yeast Nitrogen Base (YNB) (Art Nr. Y0626-2506, Sigma)

β -Mercaptoethanol (Art Nr. MG3148-25ML, Sigma)

Media and Buffers list

Table 2-1 Yeast Growth Media

<p>Yeast Peptone Dextrose (YPD)</p>	<p><u>Plates:</u> 12 g Glucose (2%), 12 g Peptone (2%), 6 g YNB (1%), are dissolved in 300 ml ddH₂O with help of magnetic stirrer at room temperature (RT). The pH of solution is adjusted to (5.5) with 37% N HCl solution. The final volume is then completed to 600 ml with deionized and distilled (ddH₂O). To prepare agar plates, a 10 g of Agar-Agar Kobel is added to the media solution. Media is then autoclaved at 121°C for 15 min. Autoclaved media is poured into plates and left solidify overnight under sterile hood. Next morning, media plates are stored at -4°C and ready to use.</p> <p><u>YP stock:</u> 12 g Peptone (2%), 6 g YNB (1%) are dissolved in 300 ml of ddH₂O, with magnetic stirrer at RT. The pH is adjusted to (5.5) using 37% N HCl solution. The final volume is completed to 540 ml with ddH₂O and media is autoclaved at 121°C for 15 min. The YP-stock can be stored at RT.</p> <p><u>YPD-rich (2% glucose):</u> a 1:10 of 20% filter-sterile glucose is prepared in YP volume according to final amounts required for experiments, by this a YPD media with a final concentration (2%) of dextrose (glucose) is obtained.</p> <p><u>YPD-starvation (0.3% glucose):</u> a 1:10 of 3% filter-sterile glucose is diluted in YP according to volume required for experiments to obtain a final</p>
--	---

Materials and methods

	concentration (0.3%) of glucose.
YPD-G418	Similar to YPD plates, except that the autoclaved media is left to cool to 50°C under continuous magnet stirring, then the media is supplemented with 200 mg/L Genticin or any other selection antibiotics. Stirred 3 min with magnet to disperse the antibiotic. Media is now ready to be poured immediately in petri-dishes. The plates are left to solidify overnight and stored at 4°C up to 1 month.
Yeast Peptone Glycerol (YPG)	YP-(0.3% glycerol): add 60 ml of 30% Glycerol (autoclaved 30% glycerol stock) – added after autoclave of 540 ml YP-Agar.
Oleic acid induction media	<p><u>Plates:</u> 0.17% Ammonium sulfate, 0.1% Yeast Extract, and 0.5% amino acid mixture. Next, 0.1% oleic acid (112 µl) is emulsified in 1 ml water and 0.5% Tween 40 (0.5 g) and vortexed. Then all of the emulsified oleic acid is added to media content. The pH is adjusted to 6.0 and final volume is adjusted to 100 ml with ddH₂O. Two grams of Agar-Agar Kobel are added and media is stirred 5 min with magnet. Media is autoclaved at 121°C for 15 min and poured on plates. Oleic acid containing media should always be stored away from light overnight at RT, then store at 4°C for up to 4 weeks. Protect from light!</p> <p><u>Media:</u> prepared the same way as the Oleic acid containing agar plates, except that no agar is added. Stored away from light at RT up to 3 weeks!</p>

Materials and methods

Synthetic Deficient (SD) - URA media	<p><u>Plates:</u> 6 g YNB (Sigma), 0.5 g Aminoacid-URA, 12 g of water-free glucose (ROTH) are dissolved in 300 ml ddH₂O, by help of magnetic stirrer, and pH is adjusted to 6.0 with NaOH. The final volume is then completed to 600 ml with ddH₂O and 10 g of Agar-Agar Kobel (ROTH) is added. Media is then autoclaved 121 °C for 15 min and poured into petri-dishes (SARSTEDT). Plates can be left overnight to solidify in sterile hood and they can be stored at 4°C for later use up to 1 month.</p> <p><u>Media:</u> 6 g 0.1% YNB (Sigma), 0.5 g Aminoacid-URA are dissolved in 300 ml ddH₂O by help of magnetic stirrer, and pH is adjusted to 6.0 with NaOH. Final volume is than completed to 540 ml by ddH₂O and media is autoclaveed at 121°C for 15 min. Prior to experiment 20% glucose filter sterile stock is diluted in media to get an SD-URA with final glucose concentration of 2% glucose.</p>
---	--

Table 2-2 Yeast Competent cells and transformation buffer

SORB Buffer	<p><u>500 ml:</u> 100 mM LiOAc (5.1 g), 10 mM Tris-HCl pH 8.0 (5 ml from 1 M stock), 1 mM EDTA pH 8.0 (1 ml from 0.5 M stock), 1 M Sorbitol (91.1 g, molecular biology grade) dissolved in ddH₂O. SORB buffer is sterile filterate and aliquoted into 50 ml falcons. The buffer can be stored at RT for up to 6 months.</p>
--------------------	--

Materials and methods

<p>PEG COMP Buffer</p>	<p><u>100 ml</u>: 100 mM LiOAc (1.02 g), 10 mM Tris-HCl pH 8.0 (1 ml from 1 M stock), 1 mM EDTA pH 8.0 (200 µl from 0.5 M stock), 40% PEG-4000 (Sigma) dissolved in ddH₂O. Sterile filterate buffer, can be stored at 4 °C for 6 months.</p>
<p>Carrier DNA (salmon sperm single stranded DNA)</p>	<p>200 mg ssDNA (Sigma) is dissolved in 20ml sterile TE Buffer (10 mM Tris-HCl pH 8.0, 1 mM EDTA pH 8.0) by vortexing or magnetic stirring in 50 ml falcon for few hours at 4°C. It is possible to use 25 ml wide bore Pipette to pipette DNA up and down until no DNA is seen. No sonication needed. The solution is can be aliquoted in volumes of 1 ml in 1.5 ml Eppendorf sterile tubes, then stored at – 20 °C. The carrier DNA must be boiled 5 min and chill immediately on ice before use. Denatured sssDNA can be boiled 3 - 4 times without significant loss of activity.</p>

Table 2-3 Genomic DNA isolation buffers

<p>gDNA lysis Buffer (LiOAc)</p>	<p>200 mM LiOAc, 1% SDS in ddH₂O.</p>
<p>Ethanol</p>	<p>96% - 100% and 70% Ethanol in ddH₂O.</p>

Table 2-4 Antibody immunofluorescence reagents

<p>Paraformaldehyde fixation (10%)</p>	<p>35 ml of 37% formaldehyde is added in a 50 ml falcon tube and the volume is adjusted to 50 ml with 1xPBS (Dulbecco). Aliquots into 5 ml volumes (in 15 ml falcons) can be saved and freezed at -20°C. Fresh aliquots are used in each experiment and stored for reuse at 4°C for up to 1 week.</p>
<p>Permeabilization (0.5% Triton-100x in PBS)</p>	<p>50 ml 1xPBS is added in 100 ml cylinder tube. A cut blue pipette tip (1000 µl) with scissor are prepared, and reverse pipetting technique is used to add 500 µl 100% Triton-100x to the 50 ml 1xPBS. The solution is then stirred with magnet for 5 min and volume is adjust to 100 ml. Final solution is then stirred for 2 min at RT and stored in 100 ml bottles at RT for later use.</p>
<p>Blocking solution (10% BSA)</p>	<p>5 g BSA is added to 25 ml 1xPBS (Dulbecco). The tube should be inverted up and down to hydrate BSA powder. The solution is put at -20 °C and carefully observed to avoid freezing, this takes approximately 10 min until all BSA powder is completely dissolved. The -20°C step can be repeated with increasing PBS volume between each 10 min at -20°C. It takes 15 – 30 min max to dissolve all BSA. The final volume is then completed with 1xPBS to 50 ml, and the solution can be aliquoted into 2 ml volume. These aliquots can be stored at -20 °C for later use.</p>

Materials and methods

Antibody Dilution Buffer (2% BSA)	2.5 g BSA is added to 25 ml 1xPBS (Dulbecco). The tube should be inverted up and down to hydrate BSA powder and incubated in -20°C for 10 min. The solution is brought back to -20°C and carefully watched to avoid freezing till BSA powder is completely dissolved. The final volume is then completed with 1xPBS to 50 ml. The solution can be aliquoted into 2 ml volume and frozen at -20°C.
1xPBS wash solution	<p><u>10x PBS stock solution:</u> In 800 ml ddH₂O: 80 g NaCl, 2.0 g KCl, 14.4 g K₂HPO₄, 2.4 g KH₂PO₄ are dissolved. pH is then adjusted to 7.4 and a final volume of 1 L is obtained by addition of ddH₂O. Final solution is sterilized by autoclaving at 121 °C for 15 min and stored at RT.</p> <p><u>1xPBS:</u> Prepare 1:10 in ddH₂O and keep at RT.</p>

Table 2-5 Nanobody staining reagents

Paraformaldehyde Fixation (4%)	Commercial reagent (Affymetrix) 4% PFA in PBS can be directly used or a 3.7% PFA can be prepared as follows: 5 ml of 37% formaldehyde is added to 50 ml falcon tube and volume is adjusted to 50 ml with 1xPBS (Dulbecco), mixed properly and saved in aliquots (5 ml aliquots in 15 ml falcons). PFA solutions can be stored at -20°C for longer times and fresh aliquots can be stored at 4°C and reused up to 1 week.
---------------------------------------	--

Materials and methods

Permeabilization	0.5% Triton-100x in PBS
PBS-T	<u>1 L</u> : 1xPBS + 0.1% Tween 20
Blocking solution (4% BSA in PBS-T)	2 g BSA powder is dissolved in 25 ml PBS-T. First vortex so that PBS-T reach the BSA powder, then incubate the mixture for 10 min at -20°C to enhance the BSA to dissolve quicker. Volume is then adjusted to 50 ml, vortex, and aliquots prepared in 2 ml Eppendorf tubes. Aliquots can be store at -20°C and used once, then discarded after use.

Table 2-6 Western blot and co-immunoprecipitation (CoIP) solutions and buffers

1.5 M NaCl	8.76 g NaCl is dissolved in 100 ml ddH ₂ O and stored in 50 ml falcon tube at RT. NaCl solutions should not be stored in Glass Containers.
10% NP-40 stock	A 1:10 dilution is prepared from 100% NP-40 (Sigma) in ddH ₂ O and kept at RT.
2 M DTT, -20°C stock frozen	3.09 g DTT is added to 6 ml ddH ₂ O, mixed properly and the final volume is adjusted to 10 ml. Stock solution is dispensed into 1ml aliquots (1.5 ml Eppendorf tubes) and stored at -20°C. The solution is stable for up to 1 year.

Materials and methods

1 M Tris-HCl stock (pH 7,4)	<p><u>1 L</u>: 121.14 g Tris (ROTH) is dissolved in 800 ml ddH₂O. pH is then adjusted to 7.0 with the appropriate volume of concentrated HCl. The final volume to 1 liter is adjusted with ddH₂O. Solution is then autoclave and stored at RT.</p>
50 mM PMSF (freshly made in case of quantitative results or low abundant proteins. Otherwise, it can be stored at -20 °C and reused for up to few month)	<p>In 50 ml Flacon tube: 0.174 g PMSF powder is weighed and 20 ml pure Ethanol is added to the PMSF. Solution is vortexed (intermediate speed), to dissolve PMSF. For safety precautions: all steps are performed under the hood with proper ventilation, because PMSF is hazardous. The PMSF should be always freshly prepared prior to use, because it is unstable in aqueous solution with a short half-life in aqueous solution (30 min).</p>
25x Complete Protease Inhibitor	<p>One tablet is added to 1 ml ddH₂O in 2 ml Eppendorf tube. The solution is vortexed and mix to dissolve the tablet. Another 1 ml ddH₂O is added to obtain 25x Complete Protease Inhibitor cocktail and stored at -20 °C. It can be used up to 3 times (3 freeze-thaw cycles) and it must be kept on ice after thawing. In some cases, it maybe better to prepare it fresh each experiment.</p>
Radio Immuno Precipitation Assay (RIPA) Buffer	<p>20 mM Tris-HCl (1 M stock) , pH 7.4, 150 mM NaCl (1.5 M stock), 2 mM EDTA (Commercial 0.5M stock), 1% NP40 (10% Stock Solution), 1 mM DTT (2 M DTT stock), 0.1 mM PMSF (50 mM Stock), 1x Complete Protease Inhibitor (25x stock freshly prepared)</p>

Materials and methods

<p>SDS-Laemli Buffer (4x)</p>	<p><u>4x stock</u>: 40% Glycerol, 240 mM Tris/HCl pH 6.8, 8% SDS, 0.04% bromophenol blue 5% β-mercaptoethanol. Store at -20°C for longer storage.</p>
<p>PBS-T</p>	<p><u>1 L</u>: 1xPBS + 0.1% Tween 20.</p>
<p>SDS Running Buffer (10x stock)</p>	<p><u>1 L</u>: Dissolve 30.0 g of Tris-base, 144.0 g of glycine, and 50 ml of 20% SDS in 1000 ml of ddH₂O. The pH of the buffer should be 8.3 (i.e. no pH adjustment is required). The running buffer should be stored at room temperature and diluted to 1X before use.</p>
<p>Transfer Buffer (10x stock)</p>	<p><u>1 L</u>: 3.03 g Tris-base and 14.41 g Glycine are dissolved in 500 ml ddH₂O 200 ml Methanol are make up to 1000 ml. The solution is stirred with magnet and store in bottle at RT.</p>
<p>Blocking Milk Buffer (5% Milk Buffer)</p>	<p><u>50 ml</u>: 2.5 g of Milk Powder is dissolved in 25 ml PBS-T, vortexed, and then complete to 50 ml with PBS-T.</p>
<p>Antibody Dilution Buffer (1% milk Buffer)</p>	<p>The 1% milk buffer can be prepared from 5% Blocking Milk Buffer by dilution in PBS-T.</p>
<p>Wash Buffer (PBST, 0.1% Tween20)</p>	<p><u>1 L</u>: 1xPBS + 0.1% Tween 20.</p>

Materials and methods

Lysis buffer (CoIP)	RIPA buffer protocol (same Table).
Wash buffer (CoIP)	RIPA buffer protocol (same Table).
Wash buffer 2 (CoIP)	same as RIPA buffer, but 500 mM NaCl is added instead of 150 mM.

Table 2-7 Antibodies list

Antibody (Clone, company)	Host	Dilution / Fixation	Art Nr.
Catalase (human catalase, Oxisresarch)	Polyclonal (rabbit)	1:500 / 10% FA	24316
ACAA1 (ag297, Proteintech)	Polyclonal (rabbit)	1:500 / 10% FA	12319-2-AP
PMP70 (clone 70-18; a.a 644-659, Sigma)	Monoclonal (mouse) IgG1	1:500 / 10% FA	SAB4200181
PEX14 (ag0932, Proteintech)	Polyclonal (rabbit)	1:500 / 10%FA	10594-1-AP
DLP1 (clone 8, BD Biosciences)	Monoclonal (mouse)	1:100 / 10%FA	611113
MYC (911B, Cell Signaling)	Monoclonal (mouse)	1:1000 / 10%FA	2276S
GFP (Jl-8, clontech)	Monoclonal (mouse)	1:1000 / 10%FA	632381
GFP-nanoboosters ATTO647N (Chromotek)	Nanobody	1:50 / 4%FA	gba647n-100

Materials and methods

RFP-nanobooster ATTO594 (Chromotek)	Nanobody	1:50 / 4%FA	rba594-100
Secondary anti-IgG Mouse KK114 (Dianova)	Sheep anti-mouse	1:50 / 10%FA	Ab504 (AG Hell)
Secondary anti-IgG Rabbit KK114 (Dianova)	Goat anti-rabbit	1:50 / 10%FA	Ab521 (AG Hell)
Secondary anti-IgG Mouse Atto594 (Dianova)	Sheep anti-mouse	1:500 / 10%FA	Ab130 (AG Hell)

Equipment (A-Z)

Abberior 2C-STSED microscope (Abberior)

AxioCam HRm (Zeiss)

Biophotometer *Plus* (Eppendorf)

Centrifuge 5415 D (Eppendorf)

Fastblot B44 transfer apparatus (Biometra)

GPR Centrifuge (Beckman)

Imager.M1 microscope (ZEISS)

ImageQuant LAS-4000 (GE Healthcare)

Standart Power Pack P25 (Biometra)

Thermomixer compact (Eppendorf)

Other materials (A-Z)

Blotting paper (Art Nr. 4033385, In-house supply)

Cell scraper 25cm (SARSTEDT, Inc USA)

Cell STAR 12-well cell culture plate, sterile, with lid (Art Nr. 665.180, CellSTAR)

Cell STAR 24-well cell culture plate, sterile, with lid (Art Nr. 662.160, CellSTAR)

Cover slides 76x26 mm (Thermoscientific)

Cover slips 12 mm (Thermoscientific)

Nitrocellulose membrane Amersham™ Protran™ 0.45 mm (Art Nr. 10600002, GE Healthcare)

Petri dishes for agar plates (Art Nr. 82.1472, SARSTEDT)

2.2. Methods

Preparation of Yeast competent cells

Competent yeast cells were prepared according to a previously described method [99].

Yeast genomic integration

Genomic integration is used to integrate or replace genetic materials in the genome of yeast cells by homologous recombination [100]. Universal cassettes have been developed to make genomic integration a straight-forward procedure, which involves a PCR amplification step of selection marker and desired genetic material (tags or promoters) from cassettes using primers that include genetic homologous recombination sequence similar to insertion or deletion sites in the genome, more details about the technique can be found in this reference [100].

To delete *pex3* in GFP-PEX35 overexpression strain (natNT2-TEFprom-GFP-PEX35), a compatible deletion cassette was used (pFA6a – hphNT1) from [100]. PCR of 25 μ l was prepared using the HiFi-KAPA polymerase kit (according to manufacturer protocol with a High-Fidelity HIFI buffer; PCR program according manufacturer protocol with $T_m = 60^\circ\text{C}$). Only 1 μ l of PCR volume was used to check PCR results, and rest was saved for transformation step. Primers used for deletion are listed in (Table 2.8).

Table 2-8 Primers sequence

Primer name	Primer sequence (5' – 3')
OST1261 (S1 primer) <i>Sc.pex3</i> deletion	GTAAAAGCAGAAGCACGAAACAAGGAGGCAAAC CACTAAAAGG ATG <u>CGTACGCTGCAGGTCGAC</u>

<p>OST1262 (S2 primer) <i>Sc.pex3</i> deletion</p>	<p>5ATA TAT ATA TAT ATT CTG GTG TGA GTG TCA GTA CTT ATT CAG AGA TTA <u>ATCGATGAATTCGAGCTCG</u></p>
<p>OST1326 <i>Hs.PEX12</i> forward primer</p>	<p>GATCCAAGCTTTTATGGCTGAGCACGGGGCTCAC</p>
<p>OST1327 <i>Hs.PEX12</i> reverse primer</p>	<p>CCCGGATCCTCAGTTCTCAGGGGAGGTAGA</p>

Yeast transformation

Transformation of yeast cells was done according to [99]. Yeast cells were heat-shocked for 15 min. In case plasmid or PCR product transformed contained auxotrophic marker cells were sedimented (2 - 3 min at 500 xg), resuspended in 200µl sterile ddH₂O, and plated directly on selection plate. Only if the plasmid or PCR product being transformed contained an antibiotic selection marker, cells were resuspended in YPD and left to grow at 30 °C (180 rpm) for 4 – 6 hours, before spread on a plate with the appropriate dominant selection marker.

Nanobody staining and STED microscopy

Strains were transformed with EYFP-SKL (plasmid PST1219) and analyzed as described [101] using GFP nanobodies coupled to Atto647N (Chromotek, Planegg-Martinsried), except that coverslips were not washed prior to use. Slides

were analyzed on a custom-made STED setup described previously [77]. Images are shown as unprocessed raw data. The size of yeast peroxisomes was calculated from the images by ImageJ. Peroxisomes were selected manually and the center of mass for each peroxisome was used to find the Full-Width-Half-Maximum (FWHM), using a “FWHM_Line.ijm” (free macro designed by Vitha, Stanislav) on ImageJ (NIH). Data were plotted and t-statistics hypothesis tests were done on OriginPro v9.1.

Oleic acid growth assays

Yeast growth on oleic acid plates was described before in [54], spotting was done as follows: overnight startup cultures in YPD starvation media (0.3% glucose) were incubated at 30 °C for 16 hours and fresh inoculums were collected in the same medium and left to grow for 9 more hours into mid-log phase. Cultures were spun down, washed once with sterile distilled water and re-suspended in water at equal OD₆₀₀ of 1. Four times 2 µl spots of serially diluted cells spotted for each strain on oleic acid, YPD and YP-Glycerol plates. Plates were incubated at optimal yeast growth conditions for two days followed, while oleic acid containing plates were incubated another ~ 14 days at 4 °C prior to digital imaging.

To obtain growth curves overtime of yeast strains in oleic acid the [28] protocol was adapted and modified as follows: overnight yeast pre cultures in YPD starvation were inoculated in fresh YPD starvation media for a 9 hours' incubation period, till they reached mid log phase. Mid log yeast cultures were collected, washed twice in ddH₂O sterile water and resuspended in water again. OD₆₀₀ was measured and yeast cells were inoculated at 0.1 OD₆₀₀ in oleic acid containing medium. To construct a growth curve under oleic acid growth conditions yeast cells were spun down, supernatants were saved to measure oleic acid consumption, and cells were washed twice with water prior to OD₆₀₀ measurements. Data analysis was done using Office Excel.

Amino acid intracellular metabolomics

For quantitative analysis, equal OD units of yeast samples were collected from equal cultures of yeast growing logarithmically or stationary in synthetic defined media. Intracellular metabolites were extracted using freeze thaw in 50% methanol at -80°C according to [102]. Cell pellets were discarded and supernatants were saved for solvent speed vacuum to get rid of methanol (at 40°C for 30 min) and extracted amino acids were re-suspended in water. Amino acid concentrations were analyzed using an Onken HPLC analyzer (Onken GmbH). Results were interpreted in (log₂)-fold of change compared normalized to wild-type, and a $\Delta pex3$ (peroxisome deficient) was included strain to serve as negative control. Additional kanamycin tagged wild-type strain was used to evaluate interference from selection marker genes.

DNA cloning and plasmids

PEX13-mGFP and PEX2-mCitrine have been described previously [103]. PEX12 cDNA was used to clone PEX12 into EYFP-C1 (Clontech) or TagRFP-C1 vectors. Sticky end PCR cloning of PEX12 using HindIII and EcoRI restriction sites. The primers sequences used in PEX12 cloning are shown in Table 2.7). Restriction, ligation and bacterial transformation were done according to NEB (England) protocols. Positive clones were identified by restriction digestion and sequencing. DNA sequencing was done using the BigDye kit (ABApplied Biosystems) and analyzed by a sequencer (chromatograph analyzer).

Patient-derived skin fibroblast

Eight ZSS patients from seven different complementation groups (*PEX1*, *PEX2*, *PEX5*, *PEX6*, *PEX10*, *PEX12* and *PEX13*) were included in the study. The diagnosis had been established by characteristic clinical and molecular findings [40, 103, 104]. A written informed consent was obtained from guardians of all patients.

Cell culture, transfection and immunofluorescence

Cells were cultured in low glucose Dulbecco's Modified Eagle Medium (DMEM) medium (Biochrom GmbH, Germany) supplemented with 1% Pen/Strep (100 units/ml Penicillin and 100 µg/ml Streptomycin, material section), 1% (w/v) glutamine (material section) and 10% (v/v) Fetal Bovine Serum (FBS) in 5% CO₂ at 37°C. For all experiments cells were detached with Accutase® (Life Technologies, material section), washed once with PBS Dulbecco (Biochrom GmbH, Germany), and counted using Neubauer hemocytometer (material section), according to manufacturer protocol. Equal densities of cells for all conditions and cell lines were seeded and cell culture conditions were kept constant to ensure maximal reproducibility. In Rescue experiments, cells were transfected using Effectene® transfection reagent (QIAGEN) according to manufacturer protocol. Medium with transfection reagent was changed after 6-8 hours and cells were incubated for 24 hours before being used in downstream experiments. For immunofluorescent detection of peroxisomal catalase [40], a rabbit polyclonal antibody against catalase (Table 2.7) was used to probe peroxisomal catalase and a donkey anti-rabbit secondary IgG antibody conjugated to Cy3 Rhodamine dye (Jackson ImmunoResearch, 1:400) for fluorescent microscopy detection. For STED experiments cells were fixed using 10% paraformaldehyde freshly prepared (Table 2.4) from a 37% formaldehyde stock (material section), blocked in 10% Bovine Serum Albumin (BSA) in PBS, and permeabilized using 0.5% Triton-100x in PBS (Table 2.4). The following primary antibodies were used: monoclonal mouse anti- PMP70 (Table 2.7), polyclonal rabbit anti-PEX14 (Table 2.7), polyclonal rabbit anti-catalase (Table 2.7), polyclonal rabbit anti-ACAA1 (Table 2.7), monoclonal mouse anti-DLP1 (Table 2.7), monoclonal mouse anti-GFP (Table 2.7), and monoclonal mouse anti-Myc (Table 2.7). Primary antibodies were incubated in 1%BSA in PBS for 1 hour at 37°C. The proteins were tagged with indirect immunostaining using the following secondary antibodies diluted in 1% BSA in PBS: Sheep anti-mouse immunoglobulin (Dianova) coupled to Atto594 (Atto-TEC, Table 2.7) or KK114

(Abberior, Table 2.7). Secondary antibodies were added in 1% BSA in PBS for 1 hour at 37°C. Cells were washed three times (10 min each) in PBS between each antibody incubation and mounted on Mowiol mounting medium.

Nanoboosted GFP and RFP in HeLa cells

HeLa cells were cultured in low glucose DMEM similar to HSF cells in 5% CO₂ at 37°C and trypsin (materials section) was used to detach adherent cells. Single transfection experiments were done using Effectene; however, for co-transfection LipofectamineLTX PLUS (Thermofisher) was used according to manufacture protocols. For nanobody staining the Chromotek nanobody protocol was used (Table 2.5) and following nanobody boosters were used GFP-Atto647N and RFP-Atto594 nanobooster (Table 2.7).

Widefield microscopy

Widefield images were obtained using the 100x oil objective (1.3 NA) of a Zeiss Imager M1 fluorescence wide field scope microscope equipped with the Zeiss AxioCam HRm Camera and Zeiss Axiovision 4.8 acquisition software. ImageJ software (NIH, USA) was used for linear contrast enhancement of images, cropping and scale bars. Images were arranged in figures using Adobe Illustrator software.

STED microscopy setups

A custom made gated STED (gSTED) setup was used for single as well as two color imaging as in previous studies [77]. For the RFP/GFP co-transfection experiments with nanobody labeling a commercial two color STED setup (Abberior™ Instruments) was used instead. Both setups use a pulse gated 775 nm doughnut shaped STED laser beam, 590 nm laser to excite Atto594 dyes and a 640 nm laser to excite Atto647N/KK114 dyes. Crosstalk was always measured

as previous using single dye labeled samples [77]. Inspector acquisition software (written by Dr. Andreas Schönle, Max Planck Institute for Biophysical Chemistry, Göttingen, Germany, available via Max-Planck-Innovation GmbH, Munich, Germany) was used on both setups and acquisition parameters kept constant for quantitative measurements. To visualize images in figures, raw images were linearly scaled in ImageJ and arranged with Adobe Illustrator.

Subdiffraction size analysis

Raw data were handled in ImageJ, smoothed with 1 pixel Gaussian function and line scans were obtained using the line drawing tool in ImageJ through structures of interest. Line scan data were copied into Matlab (www.mathworks.com) and processed for data fitting (Gaussian function) using custom-made automated routine (see Appendix 6.1). Histogram and boxplot diagrams and statistics were produced and calculated in Matlab.

CellProfiler: automated STED analysis

Images were analyzed using a *CellProfiler* (www.cellprofiler.org) pipeline designed based on previously published methods [98]. Raw images were smoothed using average 3x3 ImageJ smooth function. Gaussian blurring with a diameter of 100 nm was applied to images in CellProfiler, in order to identify single ghost structures into clusters (objects) within this diameter. Blurred images were divided into 50x50 pixel blocks and adaptive Maximum Correlation Threshold (*MCT*) algorithm (*lower limit 0.05 – upper limit 1*) was computed for each block. Shape and local maxima were used to distinguish borders, and to identify and declump grouped clusters. Holes within identified objects were filled after thresholding and declumping.

To find individual protein clusters within cluster groups, raw images were thresholded by computing two-class global *Otsu* thresholding (upper limit: 0.12 – lower limit: 1) with automatic smoothing settings. Intensity and local maxima were used to identify and declump clusters. Relating clusters before and after

Gaussian using Relate object module allowed us to identify children clusters (PMP70 clusters in the original STED image) per each parent (Ghost clusters in the blurred image). Other object features, like cluster area and eccentricity for all clusters were also calculated and saved to a spreadsheet file for further data and statistics analysis. Only blurred ghost clusters (Parent objects) with positive PMP70 cluster values from STED image (children objects > 0) were included in the downstream analysis. The analysis parameters were implemented in an automated pipeline in *CellProfiler* to ensure unbiased analysis. Boxplot, bar graphs and t-statistics tests were done using OriginPro v9.1 software and figures were arranged in Adobe Illustrator. Analysis was done on at least 3 independent experiments. However, for a number of conditions, as indicated in the figure legends, the cells have very slow division rates, and therefore only two independent experiments were performed.

***CellProfiler*: ghost peroxisomes quantification**

Images were acquired by the M1-Imager wide-field microscope with 100x oil objective (semi-automated analysis). Images were saved in ImageJ as color images (RGB). Color images were separated into respective channels in *CellProfiler* and named accordingly. The nuclei and peroxisomes were found and segmented by a primary object identification module, whereas cell borders (semi-automated analysis) were manually defined with the manual free drawing object module. Peroxisome signals were thresholded using Otsu threshold and segmented by intensity automatic settings. Nuclei were smoothed with Gaussian filter prior to segmentation to remove nuclei speckles and improve segmentation efficiency. Finally, a relate object module was implemented to quantify the peroxisome number per cell. Data analysis was done using OriginPro v9.1 statistics software. Figures were arranged on Adobe Illustrator.

Protein extraction by non-ionic detergents

Non-ionic detergent-based cell lysis, protein extraction from mammalian cell culture and SDS-PAGE techniques have been described previously [105]. Cells were lysed and protein extraction was performed as follows: cells were washed once with 1x PBS, trypsinized for 5 min at 37°C. After trypsinization, FBS containing DMEM media was added to block trypsin activity. Cells were then sedimented by centrifugation (1000 rpm, 15 min, 4 °C), washed once with 1x PBS. Then, RIPA buffer (Table 2.6) was added to cells (incubated 30 min at 4°C with vortex max. speed). Cell debris were removed by 14000 xg centrifugation and supernatant, which contain lysates, was transferred to new low protein binding polymer 1.5 ml cups. Total protein quantification using a commercial BCA assay kit (materials) was directly done and proteins were diluted to a final protein concentration in RIPA buffer. Finally, 1x SDS-Laemmli buffer (4x stock: 40% Glycerol, 240 mM Tris-HCl pH 6.8, 8% SDS, 0.04% bromophenol, 5% β -mercaptoethanol, Table 2.6) was used to denature protein and denaturation was completed by incubating at 70°C for 5 min. Protein solutions were directly used for Western blot or snap frozen by liquid nitrogen until later use.

Protein was loaded and mobilized on self-made SDS polyacrylamide gels 12% and 4% resolving and stacking gels, respectively, as previously described [106]. Protein pre-stained reference ladder (Thermo fisher®, P20199) was used as reference for protein size and migration. Equal protein amounts and volumes were loaded to avoid incorrect quantification errors. Gels were run in Bio-Rad Western blot chambers filled with SDS running buffer (Table 2.6) at 0.5mA/cm2 from the begin of entry into the resolving gel. Running speed was always lower in the stacking gel to allow efficient stacking of proteins and overall running time was less than 1 hour to avoid heat degradation of proteins. Semi-dry membrane transfer (blotting) of proteins was done on nitrocellulose blotting membrane (material section) in 1% SDS supplemented Transfer buffer (Table 2.6) at 1.2mA/cm2 for 1 hour 15min. To check transfer efficiencies NC blots were treated with commercial Ponceau S solution (Sigma, P7170-1L) to visualize total

proteins. Membranes were blocked by 5% Milk blocking buffer in PBS-T (1xPBS, 0.1% Tween 20%, Table 2.6) for 1 hour at RT. Prior to primary antibody incubation membrane blots were cut into multistrips to detect proteins of interest simultaneously, in order to increase quantitative output of our Western blot technique [107]. Membranes were probed using the following antibodies: PMP70 (Table 2.7) and GAPDH loading control (1:5000, ab2948, Sigma) diluted in 1% milk antibody dilution buffer (Table 2.6) and incubated overnight with rocking at 4°C. Excess primary antibodies were then washed three times by PBS-T buffer of 10-minute wash durations. Secondary antibody conjugated to horseradish peroxidase were applied and diluted in 1% milk dilution buffer for 1 hour at RT, followed by another washing step as previous. ECL or ECLplus chemilumincent kits (Thermofisher) were used to detect protein bands by immersing blots in ECL or ECLplus buffer for 3min in dark. Membrane blots were then put in transparent files and the protein ladder was marked by fluorescent permanent marker to visualize bands with a chemilumincent cameras.

Blot imaging and data analysis

Membranes were imaged by a chemilumincent doc system (LAS4000, Siemens). For quantitative purposes, exposure time was kept at a minimum to avoid signal saturation; however, exposure time was above 10 seconds to ensure linearity of detectors. Bands signals were quantitated (for densitometry) using Image Studio Software (LI-COR Biosciences). For each sample, the bands were normalized to GAPDH and results of at least three independent replicate experiments were included in the final analysis. One way anova statistics analysis was carried out for induction experiment using excel and the R-square statistics software to calculate *F-statistics*.

GFP-trap co-immunoprecipitations experiments

HeLa cells were seeded and cultured in 10 cm dishes at a density of 2.2 million/x10⁶, incubated overnight at 37°C and 5% CO₂ in low glucose DMEM medium. Next day, cells were transfected using Effectene (QIAGEN, UK) transfection reagent according to manufacturer protocol. Twenty-four hours post transfection; cells were scrapped in 1 ml cold PBS using sterile cell scraper (25cm, SARSTEDT, Inc USA) and harvested according to GFP-trap A (Chromotek) manufacturer protocol. Fresh RIPA buffer (20 mM Tris-HCl, 150 mM NaCl, 1 mM EDTA, 1x Roche cocktail inhibitors, and 0.1 mM PMSF; Table 2.6) was added to lyse cells. Cells were resuspended in RIPA using 0.45 mm x 0.5 mm needles and a 2 ml syringe. GFP trap A beads were equilibrated according to the manufacturer by dilution buffer B (Table 2.6) supplement with 1x Roche cocktail inhibitors. Lysates were incubated at 4 degrees for 90 min for trapping GFP by tumbling end over end. Bound beads were washed two times in dilution buffer and additional wash in wash buffer 2 (Table 2.6). Some lysate and unbound fraction were always saved for Western blot analysis. GFP-Protein and bound complexes were eluted from beads by boiling in 2x SDS buffer for 5min. One tenth of lysate volume of bound and unbound fractions was loaded on SDS-PAGE. Western blot SDS-PAGE analysis was carried out as previously. Multistriped membranes IP lanes were probed using GFP (Abcam, Table 2.7) and PMP70 (Sigma, 1:500; Table 2.7). Proteins of interest were detected with HRP-conjugated donkey anti-rabbit IgG antibody (1:5000, Invitrogen) and donkey anti-mouse IgG antibody (1:5000, Invitrogen), and visualized with Pierce ECLplus Western blotting substrate (Thermo Scientific), according to manufacturer protocol.

3. Results

The results described in the following sections are part of two unpublished manuscripts:

1. Kareem Soliman, Fabian Göttfert, Hendrik Rosewich, Jutta Gärtner, Sven Thoms “Super-resolution imaging reveals the subdiffraction structure of wild-type and Zellweger Syndrome Spectrum peroxisomes” (*in preparation*).
2. Ido Yofe, Kareem Soliman, Silvia G Chuartzman, Bruce Morgan, Tobias P Dick, Sara J Cooper, Christer S Ejsing, Maya Schuldiner, Einat Zalckvar, Sven Thoms “PEX35 a novel regulator of peroxisome biogenesis” (*under revision*).

3.1. Characterization of PEX35: a novel regulator of peroxisome abundance

Super-resolution microscopy demonstrates opposing effects for loss or overexpression of YGR168C

The deletion and overexpression of YGR168C have been found to decrease numbers of peroxisomes per cell (Yofe et al, unpublished). Confocal microscopy revealed enlarged peroxisomal size in both deletion and overexpression of YGR168C. To analyze the effect of YGR168C on peroxisomes in more details, the peroxisomal size and morphology were analyzed by STED microscopy. Yeast strains were transformed with a GFP variant (EYFP-SKL) that is targeted to peroxisomes and cells were labeled with nanobodies directed against GFP. The size of 71 wildtype peroxisomes was measured and mean analysis revealed a peroxisomal subdiffraction diameter of 174 nm (± 8 nm s.e.m.) (Fig.3.1A).

Next, STED microscopy revealed a subdiffraction phenotype of the mutant YGR168C gene. The numbers of peroxisomes were reduced in the $\Delta ygr168c$

strain, but their sizes were slightly, but not significantly increased. However, peroxisomes in the overexpressing strain (natNT2:TEF_{prom}-PEX35 strain) revealed a convoluted subdiffraction phenotype of enlarged peroxisomes, which in some cases indicate hyper-vesiculation of tiny peroxisomes that clump together, which appear as single big peroxisomes when visualizing cells by confocal microscopy (Fig. 3.1B).

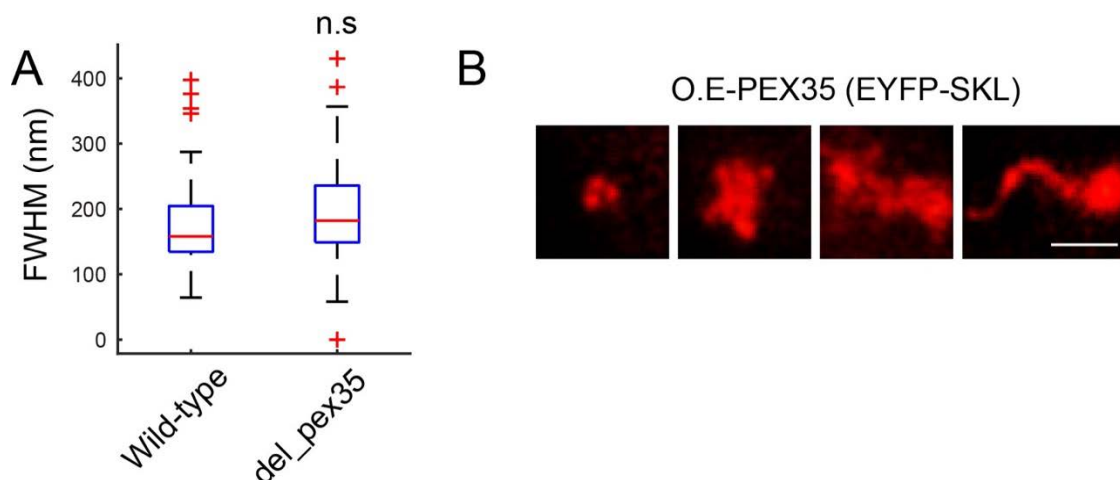


Figure 3.1 STED subdiffraction size and phenotype analysis of yeast peroxisome in Pex35 mutant strains.

STED imaging and analysis was done on yeast strains expressing EYFP-SKL and labeled with nanobody coupled to Atto647N. (A) STED line scan analysis of peroxisome size from yeast wildtype and $\Delta pex35$ strains. The boxplot indicates subdiffraction sizes of peroxisomes measured by FWHM from Gaussian fit line scans. t-statistics analysis indicated (n.s. not significant, at $P < 0.05$). (B) STED images of peroxisomes (EYFP-SKL) of the O.E.-PEX35 strain. Images are smoothed with a 3x3 average filter. Scale bar = 500 nm.

Based on these observations the YGR168C a regulator of peroxisome number and size in yeast. In addition to that, the associated YGR168C overexpression phenotype that is revealed by STED microscopy suggests a

novel role of the YGR168C protein (Ygr168c) in peroxisomal membrane vesiculation.

***YGR168C* is a new *PEX* gene (*PEX35*)**

Since Ygr168c has shown to be a new peroxisomal protein with signs of a peroxin, it was named Pex35. Most strains with defects in *pex* genes show growth defects when plated on media with oleic acid as sole carbon source [28]. Strains with a *ygr168c* gene deletion showed a reduced growth and reduced halos, representative of a lack of oleic acid consumption, while growth on glucose media was not affected (Fig. 3.2A). However, overexpression of the GFP tagged isoform (TEFprom-GFP-PEX35) showed a strong phenotype suggesting that N-terminal tagging aggravates the phenotype (Fig. 3.2A). Growth curves on oleate as a sole carbon source confirm this finding: The growth rate of *ygr168* and *TEF1prom-GFP- YGR168C* was higher than $\Delta pex3$ and less than the control (Fig. 3.2B). Quantitative assessment of oleate at the end point of the growth assay showed that mutant cells indeed utilized less of the available oleic acid (Fig. 3.2C). The loss of peroxisomal punctate localization in peroxisome defect strains (e.g. $\Delta pex3$) is a unique characteristic of bona-fide peroxisomal membrane proteins. In order to prove that it is a bona-fide peroxisomal protein, the expression of GFP-Ygr168c was tested in the absence of *pex3*. In $\Delta pex3$, GFP-Ygr168c expression is strongly reduced and the residual GFP signal is distributed in the cytosol and the ER (Fig. 3.2D), which further confirms that Ygr168c is a peroxisomal protein.

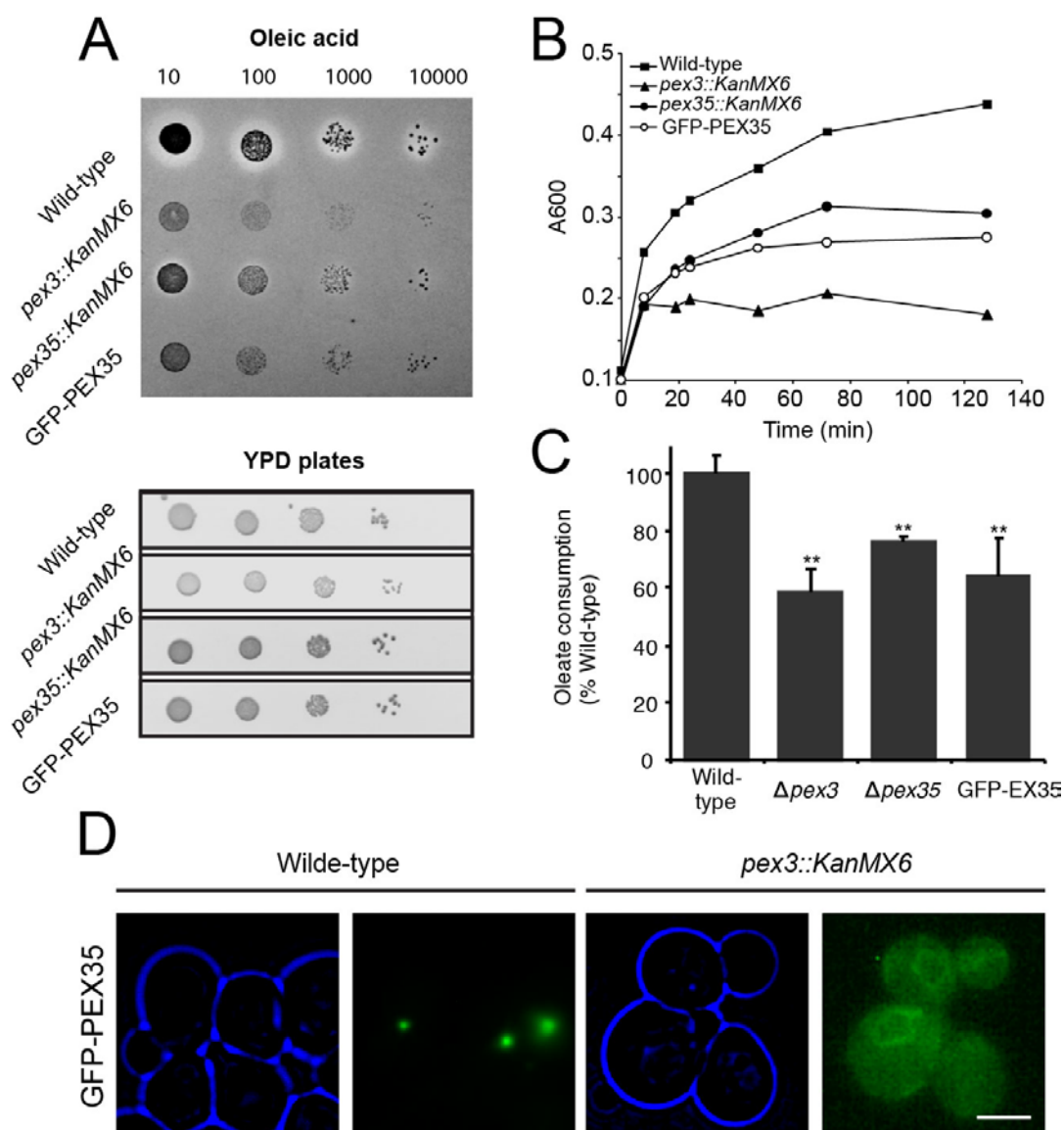


Figure 3.2 YGR168C is a new peroxin (PEX35).

(A) Oleic acid spotting assay of indicated strains (top) and their growth on YPD control plates (bottom). (B) Growth curves in oleate medium over 4 days of wildtype, $\Delta pex3::KanMX6$, $\Delta pex35::KanMX6$, and TEFprom::natNT2-GFP-PEX35 (GFP-PEX35) strains. (C) Oleic acid consumption of the yeast strains, t-statistics are indicated with their significance (**, $P < 0.01$). (D) TEFprom::natNT2-GFP-PEX35 (GFP-PEX35) localization in the wildtype (control) strain and the $\Delta pex3::KanMX6$ defect strain. Scale bar = 5 μ m.

Characterizing the molecular function of PEX35

SGA genetic lethality screen indicated a synthetic defect of PEX35 and many genes of amino acid metabolic pathways, especially that of the amino acids arginine and lysine (Yofe et al, unpublished). This initiated a metabolome study of yeast amino acids of $\Delta pex35$ and GFP tagged overexpression strains, in combination with wildtype and a peroxisome defect strain ($\Delta pex3$) as control strains. Metabolome analysis revealed altered amino acid levels in the $\Delta pex3$ strain, and in both Pex35 overexpression and deletion strains (Fig. 3.3). The changes in the arginine and citruline levels were significant: arginine was ~ 90 percent reduced in TEFprom-GFP-PEX35 strain and slightly (~ 1.65 fold) increased in the $\Delta pex35$ strain, whereas citruline was only detectable in the TEFprom-GFP-PEX35 strain (Fig. 3.3). Additionally, alanine and lysine levels were altered in the $\Delta pex3$ strain, which emphasizes the role of peroxisomes in regulating the amino acid metabolism [108, 109].

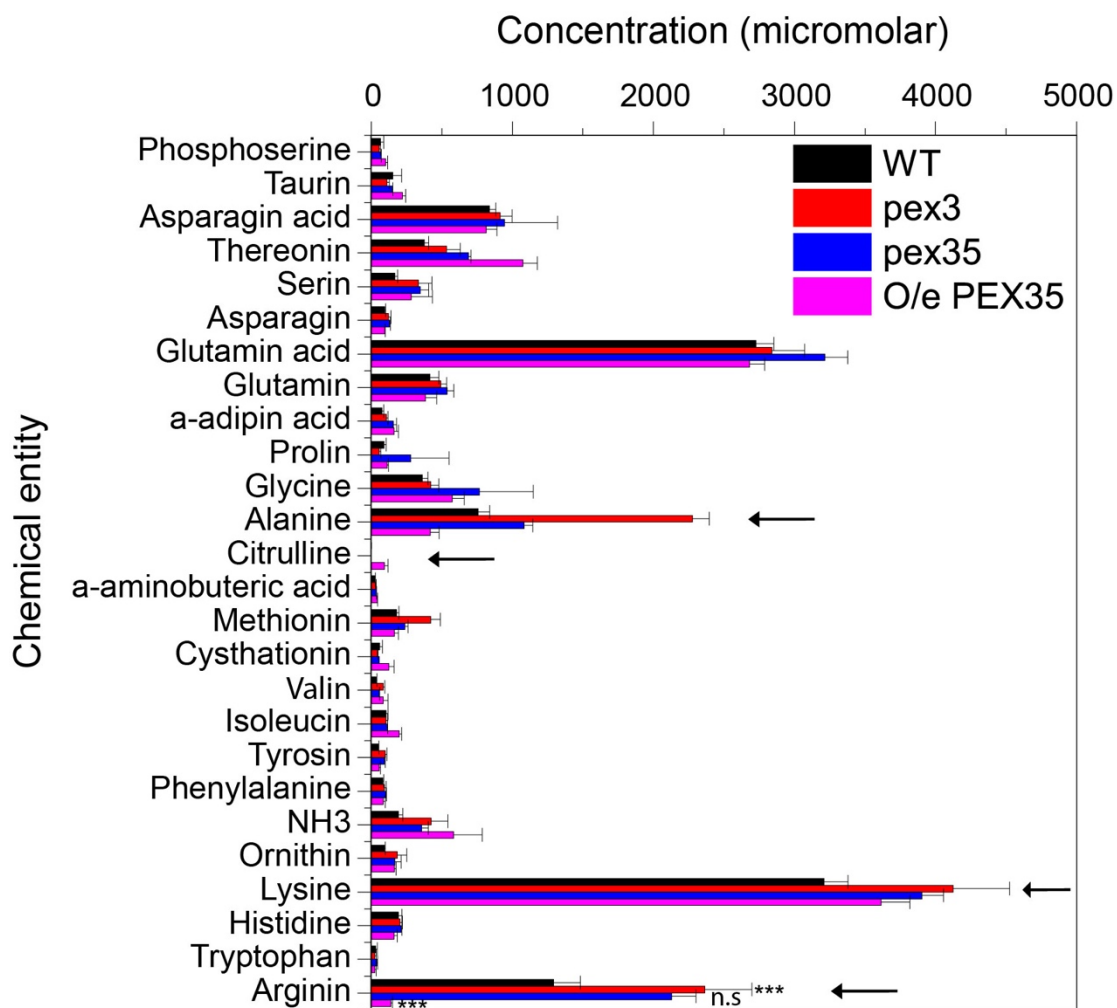


Figure 3.3. Intracellular amino acid metabolome analysis.

HPLC intracellular metabolomics analysis in wildtype (n=3), Δ pex3 (n=3), Δ pex35 (n=2), GFP-PEX35 (n=3). Arrows indicate altered amino acids in mutant strains compared to the wildtype control strain and the t-test statistics calculated and expressed (***) $P < 0.001$ and not significant, n.s).

3.2. Characterization of human peroxisomes

Peroxisome subdiffraction structure in normal and proliferating condition

Human peroxisomes appear as spherical or elongated structures distributed across the whole cytoplasm when imaged by diffraction-limited fluorescence microscopy (Fig. 3.4A). To test whether super-resolution microscopy could resolve the peroxisomal membrane relative to the lumen, the peroxisomal membranes of HSF cells were stained with anti-PEX14 antibodies and secondary antibodies coupled to Atto594. Only STED microscopy could reveal the subdiffraction membrane-vs.-lumen arrangement (Fig. 3.4B,C). The estimated diameter of peroxisome appeared to be ~250 nm in the confocal image, measured by full FWHM of the Gaussian fitted line scan (see material and methods; Fig. 3.4D). However, using STED and analyzing the same position of the peroxisome structure the diameter was only ~ 100 nm, as measured by the distance between the peaks of the Gaussian fitted line scan (Fig. 3.4E). Quantification analysis of the diameter of 90 peroxisomes labeled with PEX14 and KK114 coupled secondary antibodies revealed a mean peroxisomal diameter of 98.1 ± 1.8 nm (s.e.m) (Fig. 3.4F).

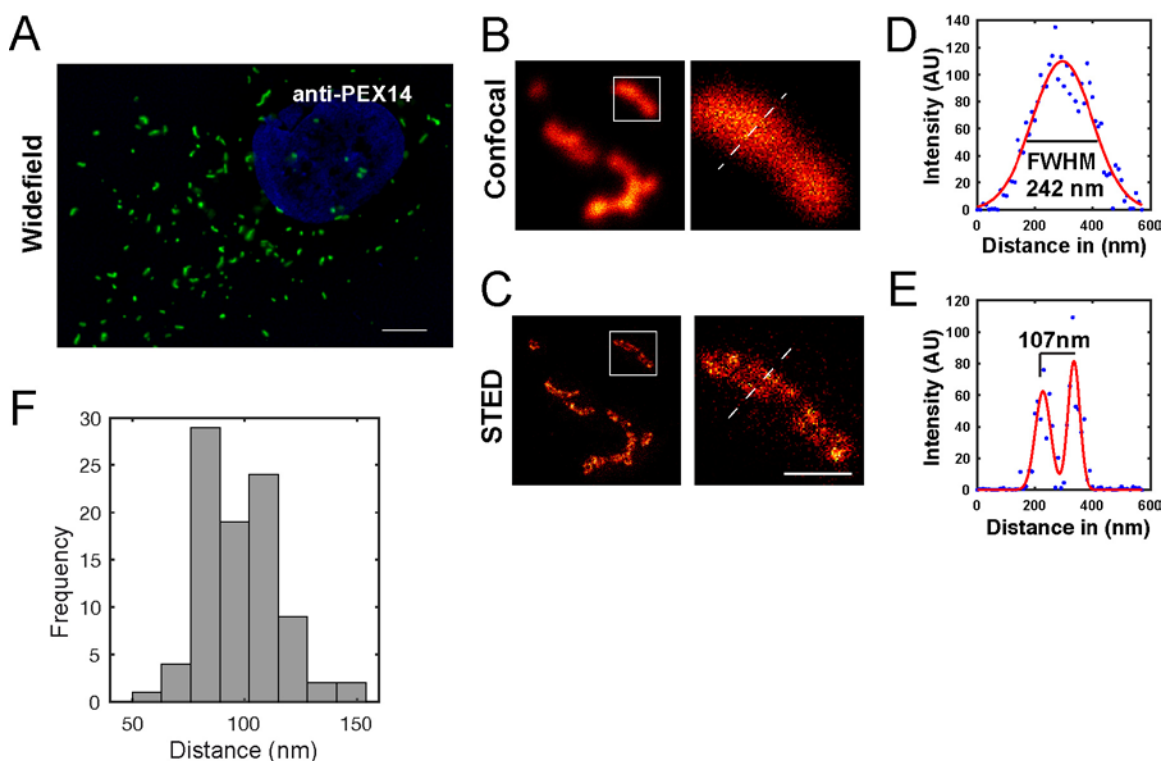


Figure 3.4 STED nanoscopy reveal peroxisome membrane and lumen.

(A) Widefield image of human skin fibroblast peroxisomes probed with polyclonal rabbit anti-PEX14 antibody and labeled with secondary antibodies coupled to the Atto594 dye. Scale bar = 5 μm . (B-C) Confocal and gSTED of the same peroxisomal structure. (D-E) Line scan analysis (Dashed lines). (F) Histogram of subdiffraction size of peroxisomes immunostained with anti-PEX14 and labeled with KK114 conjugated to secondary antibodies ($n = 90$) measured by distance from two maxima of two component Gaussian fit. Peroxisome mean diameter ($d_{\text{mean}} = 98.1 \pm 1.8 \text{ nm}$ (s.e.m.))

To visualize the peroxisome matrix, two-color STED imaging was used on peroxisomal membranes decorated with anti-PMP70 together with anti-catalase (CAT1) or anti-acetyl-CoA acyltransferase1 (ACAA1) antibodies to label the matrix (Fig. 3.5A,D). Peroxisomal membrane profiles in the microscopic plane were detected and the matrix enzymes CAT1 or ACAA1 were located within this membrane-confined space (Fig. 3.5B,D). Gaussian-fitted line scan analysis

showed matrix proteins peaks at the center of peroxisome membrane dips (Fig. 3.5C,F). Taking into account the poor Z resolution of the used STED microscope, it is remarkable that we were still able to observe PMP70 only at the lateral side of peroxisomal membrane and matrix inside the membrane of peroxisomes

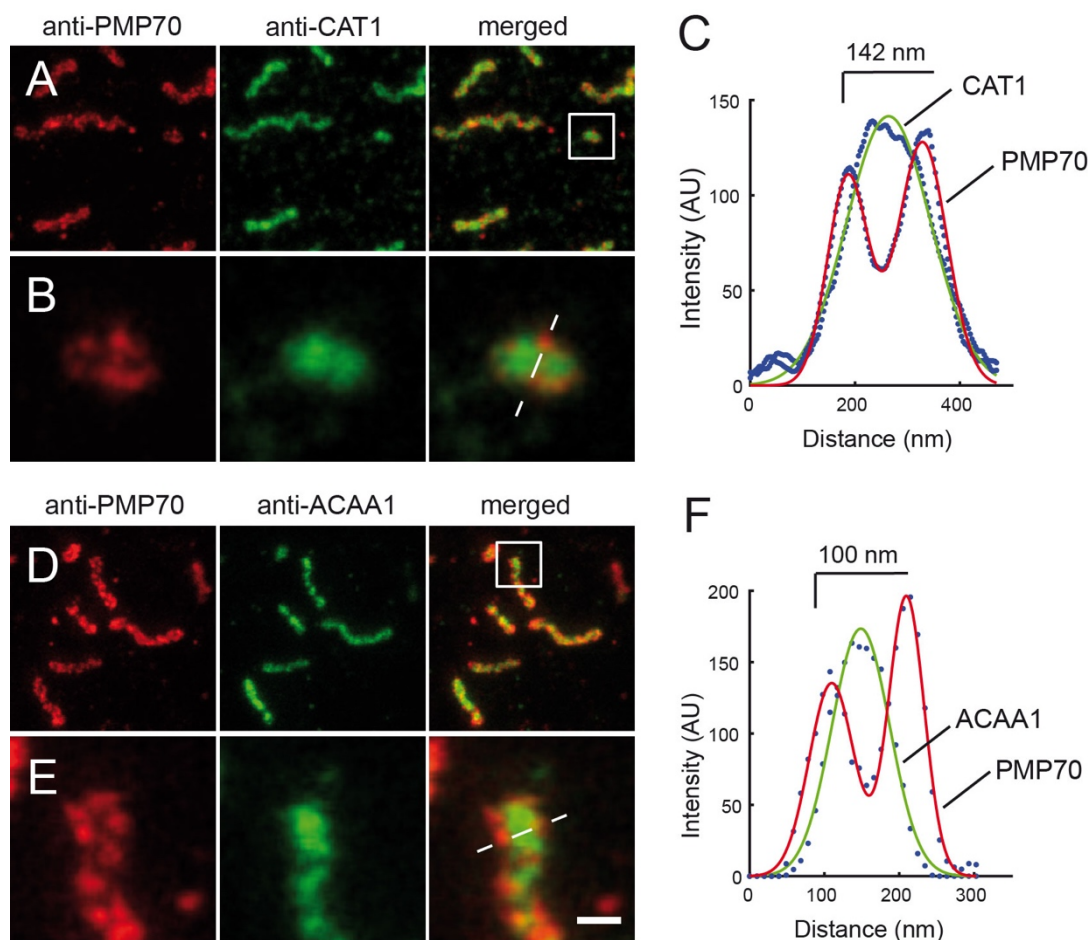


Figure 3.5 Two-color STED nanoscopy of peroxisome membrane and matrix. HSF cells double immunofluorescence (A) Monoclonal anti-PMP70 labeled with KK114 secondary in red (left), polyclonal rabbit anti-Catalase (anti-CAT1) labeled with Atto594 coupled secondary in green (middle), and a merged image of both (right). (B) Blow-up of box in (A). (C) Gaussian fit of the line scan marked in (B). (D) Monoclonal anti-PMP70 labeled with KK114 secondary in red (left), polyclonal rabbit anti-3-Ketoacyl thiolase (anti-ACAA1) in green (middle), and merged image of both (right). (E) Blow-up of one peroxisome in (D). (F)

Gaussian fit of the line scan marked in (E). Images were smoothed by 3x3 average filter and linearly scaled. Scale bar = 500 nm.

Next, the structure of hyper-tubulated peroxisomes induced by the overexpression of PEX11beta were analyzed by STED microscopy. PEX11beta-Myc expression in HeLa cells showed hyper-tubulated membrane morphologies in most of the cells 24 hours after transfection (Fig. 3.6A). STED microscopy revealed the subdiffraction size of hyper-tubulated structures to have a mean diameter of $91.8 \text{ nm} \pm 20.6 \text{ nm}$ in comparison to control peroxisomes (HeLa cells without PEX11beta overexpression immunostained with anti-PEX14 antibody), which shows a mean diameter of $94.8 \pm 21.8 (\pm\text{SD})$ (Fig. 3.6B,D). In addition, vesicular peroxisomal structures were also found that appeared to undergo fission (Fig. 3.6C). The data indicates no change in the peroxisomal diameter upon PEX11beta overexpression *in vivo* (Fig. 3.6E).

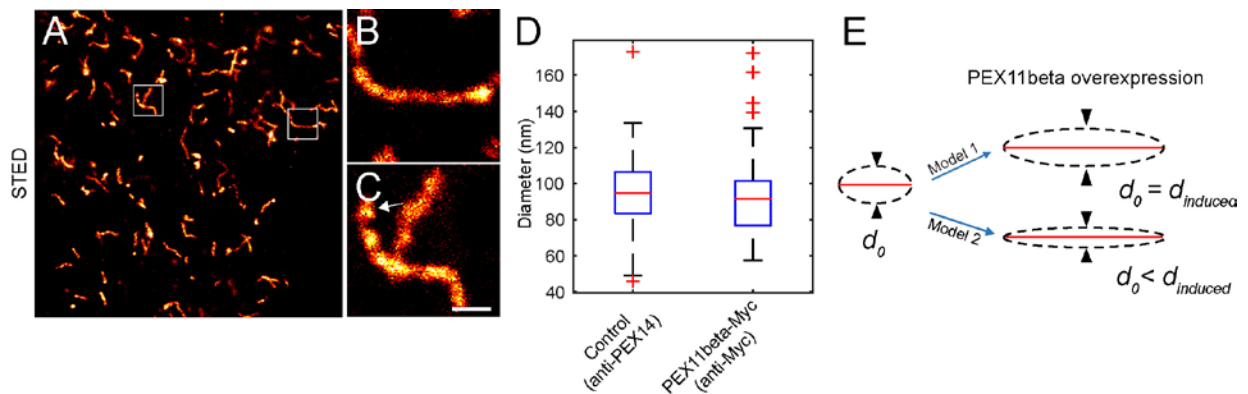


Figure 3.6 STED subdiffraction imaging of hyper-tubulated peroxisomes.

Peroxisome proliferation was induced by overexpression of PEX11beta membranes. (A) Raw STED overview image of HeLa cell overexpressing PEX11beta-Myc fusion 24 hours after transfection, probed with a monoclonal anti-Myc antibody and labeled with a secondary antibodies conjugated to KK114 dye. (B) Blow up of a hyper-tubulated PEX11beta-Myc structure. (C) Another blow up of hyper-tubulated PEX11beta-Myc structure and arrow indicate a vesicle like structure. (D) Boxplot shows the diameter distribution of $n = 74$ anti-PEX14 structures (untransfected, HeLa cells) measured by distance between

peaks of Gaussian fit membrane profiles, and diameter of $n = 88$ PEX11beta-Myc structures (tubules) measured by FWHM of the Gaussian fit (in nm). The mean diameter ($d_{\text{mean}} = 94.8 \pm 21.8$ nm and ($d_{\text{mean}} = 91.8$ nm ± 20.6 nm (\pm SD), respectively. Scale bar 500nm. (E) Model cartoon indicating PEX11beta effect on peroxisomal membrane thickness. Model 1 suggests that PEX11beta induce peroxisome elongation without constricting peroxisomal membranes (initial peroxisome diameter “ d_0 ” is equal to diameter of induced peroxisomes “ d_{induced} ”). Model 2 suggests that PEX11beta not only elongates peroxisomal membrane, but leads to membrane constriction and therefore the diameter of peroxisomes induced by PEX11beta is less than non-induced peroxisomes.

DLP1 and MFF localization on peroxisomes at the nanoscale

Peroxisomes proliferate by division employing a fission machinery that is shared with mitochondria [110]. In this study, the arrangement of two important fission proteins, DLP1 and MFF, have been examined by super-resolution microscopy. It was previously shown that a mutated form of DLP1 is able to form helical rings around constricted mitochondria and endoplasmic reticulum membranes [111]; however, such ring structures have not been reported with wild-type DLP1 *in vivo*. Anti-DLP antibody was used to visualize endogenous DLP1 in HSFs. Mitochondria were labeled with antibodies against the outer membrane protein TOM20 as a non peroxisomal control. By this approach, not only the DLP1-puncta along the mitochondrial membrane were revealed, but also rare ring structures and half-ring structures could be seen on constricted and invaginated mitochondrial membranes (Fig. 3.7).

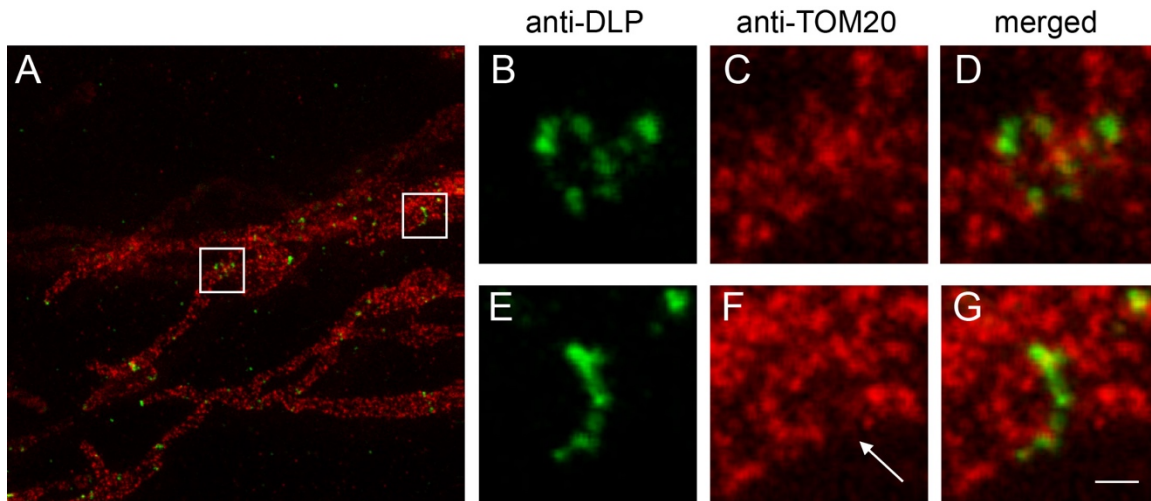


Figure 3.7 Mitochondrial wtDLP1 ring structures on mitochondrial constricted and invaginated membranes (arrow).

HSF cells immunostained with anti-DLP1 and anti-TOM20, labeled with Atto594 anti-mouse and KK114 anti-rabbit secondary antibodies, respectively. (A) STED image overview of one cell. (B-G) Blow-ups of the boxes in (A). Scale bar 200 nm.

When analyzing peroxisomes, rare constricted peroxisomal membranes that have DLP1 were found, but did not reveal DLP1 ring structures (Fig 3.8A). DLP1 was also associated with peroxisome membrane tips (Fig. 3.8B). It has previously been observed with diffraction-limited microscopy that DLP1 localizes to peroxisome tips and constriction sites of elongated peroxisomes [34]. However, diffraction-limited microscopy proved that it can easily provide misleading information about the localization of DLP1 on peroxisomes: Fig. 3.8D shows a DLP1 that appears to be located at a constriction or fission site of the peroxisome. Using STED, we had to classify these DLP1 puncta as not associated with the peroxisome (Fig. 3.8E). Taking advantage of this increase in resolution, a quantification analysis of DLP1 puncta associated with peroxisomes has been carried out. Most of peroxisomal DLP1 (89%) was found at membrane tips of peroxisomes and 11% were localized at invaginated or constricted membranes (Fig. 3.8F). To complement the image of peroxisomes undergoing fission, the MFF fission protein using GFP-MFF has been visualized.

Subdiffraction structures of GFP-MFF, marking membrane division sites of peroxisomes were identified (Fig. 3.8G,I).

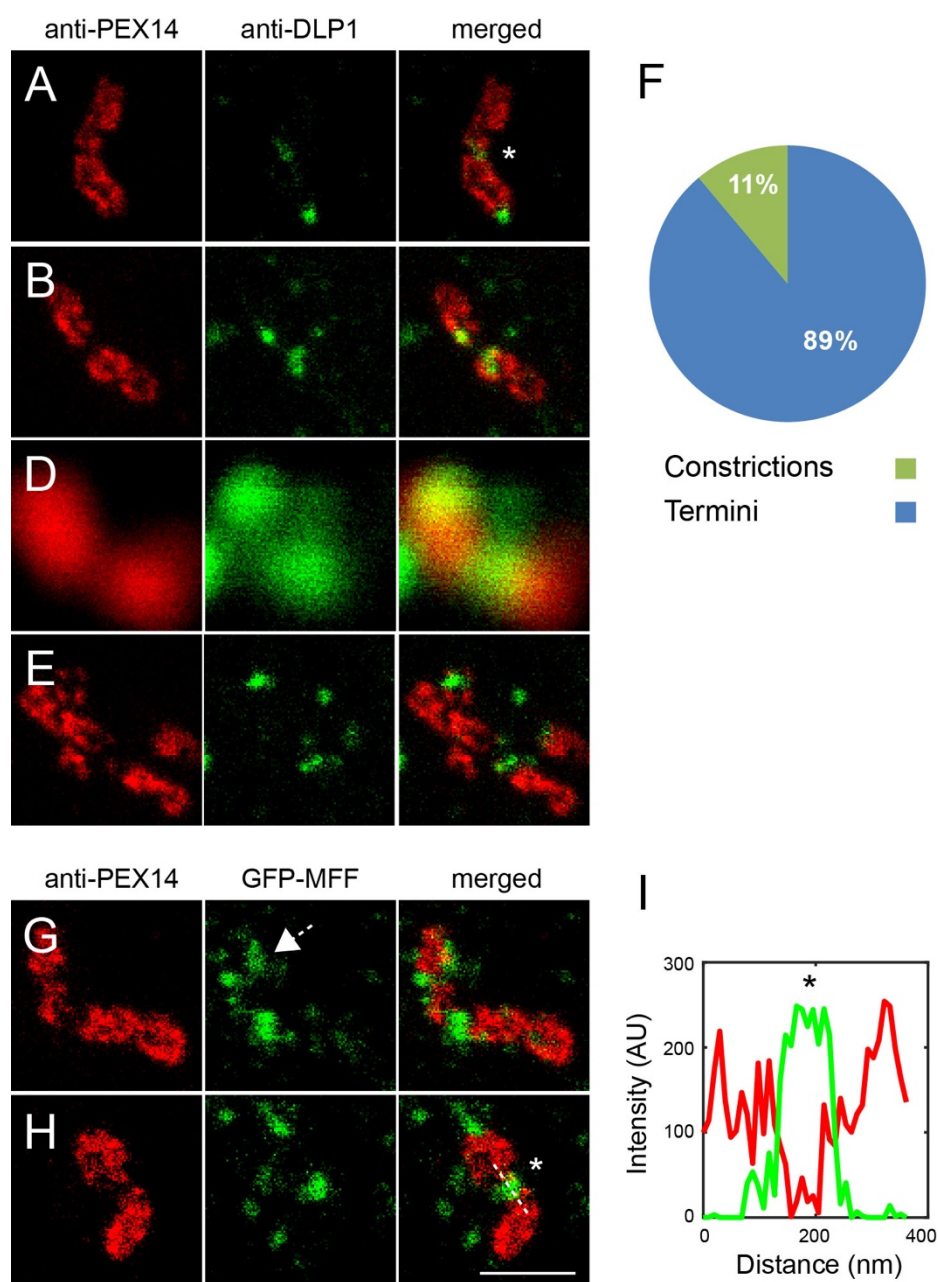


Figure 3.8 STED nanoscopy of DLP1 and MFF at peroxisomal constriction sites.

(A-B) HSF cells double immunofluorescence of polyclonal anti-PEX14 labeled with KK114 secondary (red channel, left) and monoclonal anti-DLP1 labeled with Atto594 secondary (green channel, middle), merged image (right). (D) Confocal

image of PEX14 and DLP1. (E) STED scan of the image in (D). (F) Pie plot of anti-DLP1 localization on membrane tips or middle/constricted sites of peroxisomes (n=117, positive DLP1 peroxisome structures from 5 optical sheets. (G-H) HeLa cells transfected with GFP-MFF, polyclonal anti-PEX14 labeled with a KK114-conjugated secondary (red channel, left), monoclonal anti-GFP labeled with Atto594 secondary (green channel, middle). Asterisks * indicate division sites. Arrow in (G) indicates GFP-MFF half ring structure. (I) Line scan plot of the line scan marked in (c). All images are raw STED or confocal data, linearly scaled for intensity. Scale bars 500 nm.

RING and docking subcomplexes segregate on distinct adjacent peroxisomal membrane compartments

Recent work in yeast showed that peroxisomes are formed by heterotypic fusion of PPVs carrying distinct peroxins [20]. This model implies that the RING subcomplex and the docking/translocation subcomplex targets to different PPVs before fusion. To test whether the RING and the docking complex in human cells target to distinct membrane vesicles or subdomains, transiently RFP- and GFP-tagged peroxins were co-expressed in HeLa cells. As a control, the peroxisomal localization of the peroxins-fusions were checked by testing and confirming their peroxisomal colocalization with anti-catalase (Fig. 3.9). Tagged proteins were labeled with anti-RFP and anti-GFP nanobodies coupled to STED-compatible dyes. Nanobodies are tenfold smaller than conventional antibodies and therefore offer better localization precision of their labeled antigens in combination with super-resolution microscopy. PEX2 and PEX12 of the RING complex were found to fully overlap (Fig. 3.10A), while PEX2 did not colocalize with PEX13 structures (Fig. 3.10B). At the same time, PEX14 and PEX13 of the docking complex showed full overlap (Fig. 3.10C); however, PEX12 did not show overlap with PEX13 structures (Fig. 3.10D). The analysis results indicate that the docking and RING subcomplexes localize to adjacent but distinct membrane structures.

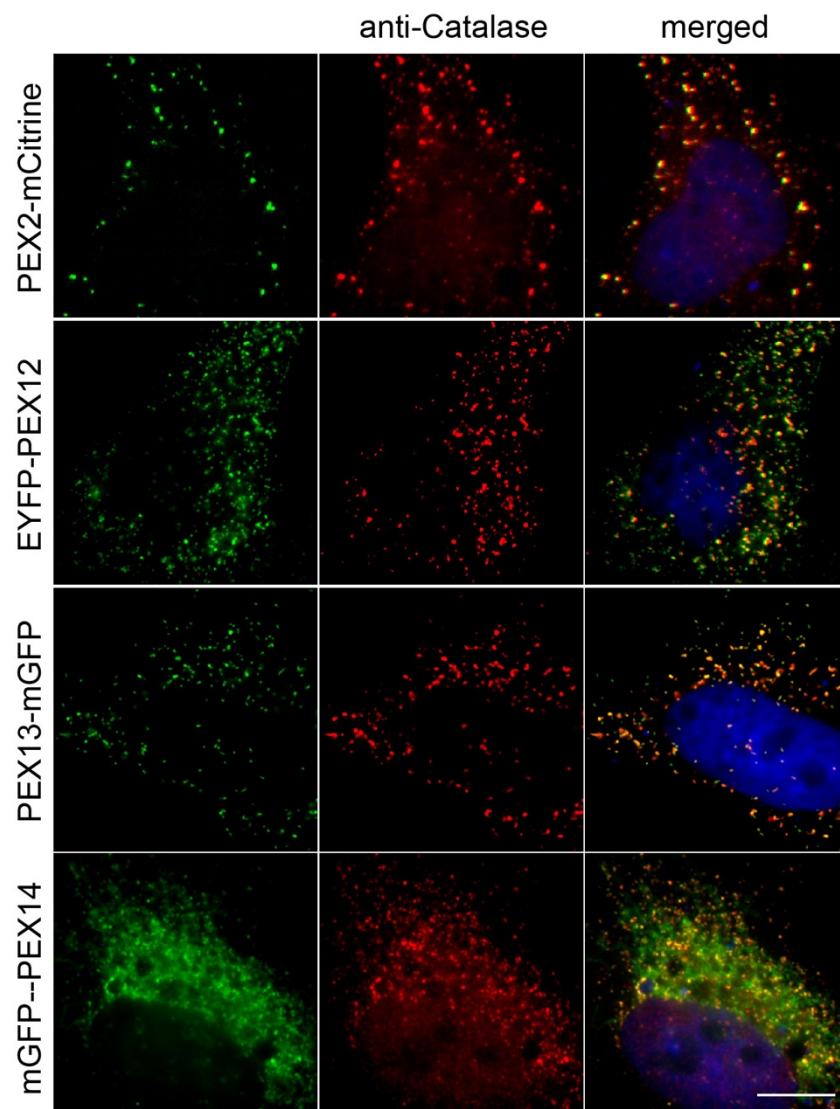


Figure 3.9 Peroxisomal localization of fluorescently labeled PEX proteins

PEX fusion proteins transiently expressed in HeLa cells for 24 hours (left column). Fixed cells processed for indirect immunofluorescence using anti-CAT1 antibody labeled by donkey anti-rabbit Cy3 secondary antibody (middle column). Overlay of both channels (right column). Scale bar = 10 μ m.

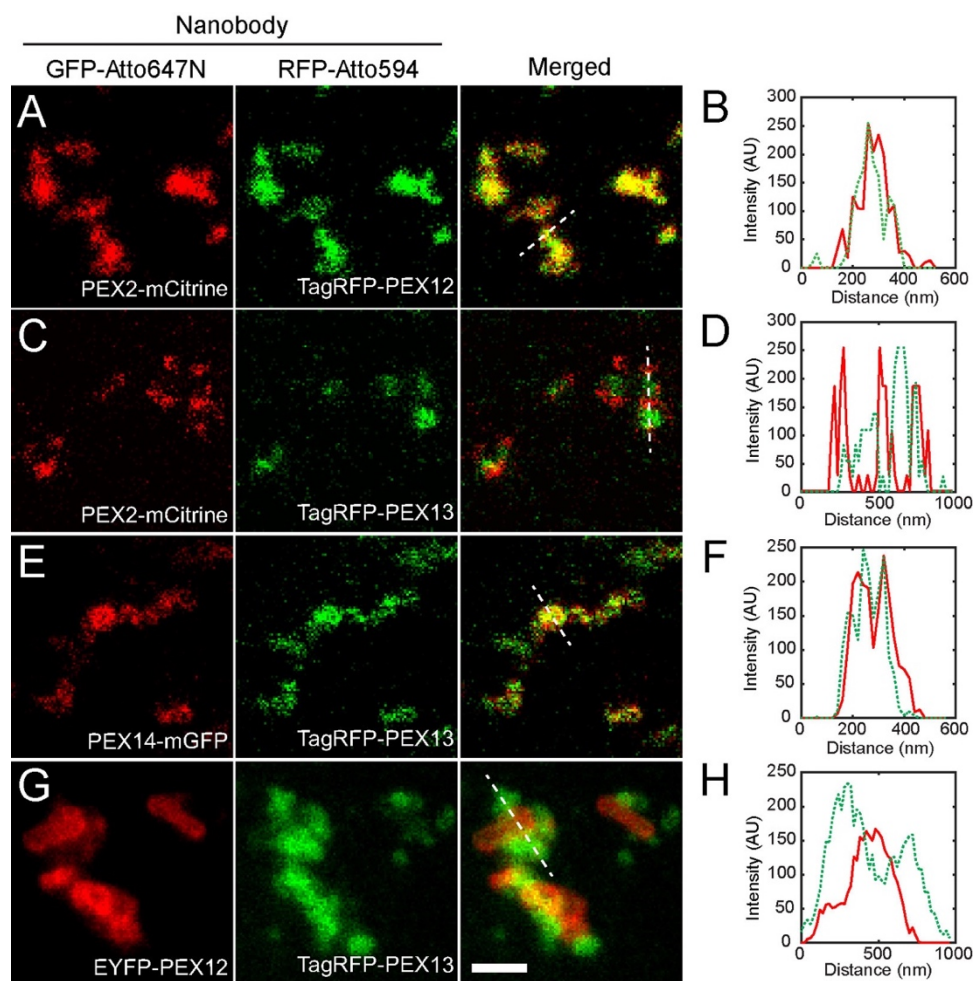


Figure 3.10 STED visualization of fluorescently tagged Docking and RING peroxins reveal distinct localization of each subcomplex on adjacent membranes.

GFP/mCitrine and RFP fusion peroxins co-transfected in HeLa cells and fixed 24 hours after transfection. Labeled with the GFP-ATTO647 and RFP-ATTO590 nanobodies against GFP/mCitrine and RFP, respectively. (A) Colocalization of PEX2-mCitrine in (red channel, left) and TagRFP-PEX12 in (green channel, middle), merged overlay. (B) Line scan analysis of the line in (A). (C) Colocalization of PEX2-mCitrine in (red channel, left) and TagRFP-PEX13 in (green channel, middle), merged overlay (right). (D) Line scan analysis of the line in (C). (E) Colocalization of PEX14-mGFP in (red channel, left) and TagRFP-

PEX13 in (green channel, middle), merged overlay (right). (F) Line scan analysis of the line in (E). (G) EYFP-PEX12 in (red channel, left), TagRFP-PEX13 in (green channel, middle), merged overlay (right). (H) Line scan analysis of the line in (G). Line scan plot: green dashed line (green channel) and red solid line (red channel). Scale bar is 500nm.

Super-resolution STED analysis of ZS ghosts

The description of residual membrane structures (ghosts) in ZS cells by EM and indirect immunofluorescence microscopy initiated their analysis with respect to the cellular phenotype [43–45]. Here, STED microscopy and automated imaging analysis (materials and methods) were used to quantify the size and morphology of peroxisomal membrane ghosts in 8 ZSS patients' HSFs (Table 3.1). In this study, eight different complementation groups with variable severity were examined by STED microscopy. Two patients with *PEX1*^{-/-} mutations were included; a milder mutation (PEX1-G843D) with residually active PEX1 protein, and another with severe mutation (PEX1-I700fs) that cause early stop codon termination and complete loss of function [112]. An HSF cell line with healthy peroxisomal biogenesis served as control. Peroxisome ghosts were stained with anti-PMP70 and ghost clusters (particles) were identified if the thresholded signals (local-maxima) were localized within a Gaussian blur diameter of 100 nm and show minimum cluster diameters of 10 Pixels (Fig. 3.11A). Clearly distinct clumped ghost clusters were divided by shape parameters (*CellProfiler*), and the areas of more than 600 clusters were analyzed per condition (Fig. 3.11B). In the analysis, the ghost structures in ZSS patient cells reveal a significantly larger area compared to wild-type peroxisomes, which can reach up to 2 times the average size of normal peroxisome (Fig. 3.11C, Table 3.1). The increasing tendency in the average size of ghosts between patients seems to correlate with the molecular function, the severity of mutation, and the residual import activity of matrix proteins (Table 3.1). Eccentricity of measured structures were also calculated, in control cells more elongated and eccentric structures were

revealed compared to ghost structures in ZSS patient cells (Fig. 3.11D). Based on this observation, it is possible to speculate that the de-tubulated structures of ghosts and their loss of membrane curvature functionally correlates with the impaired division of these abnormal structures [113].

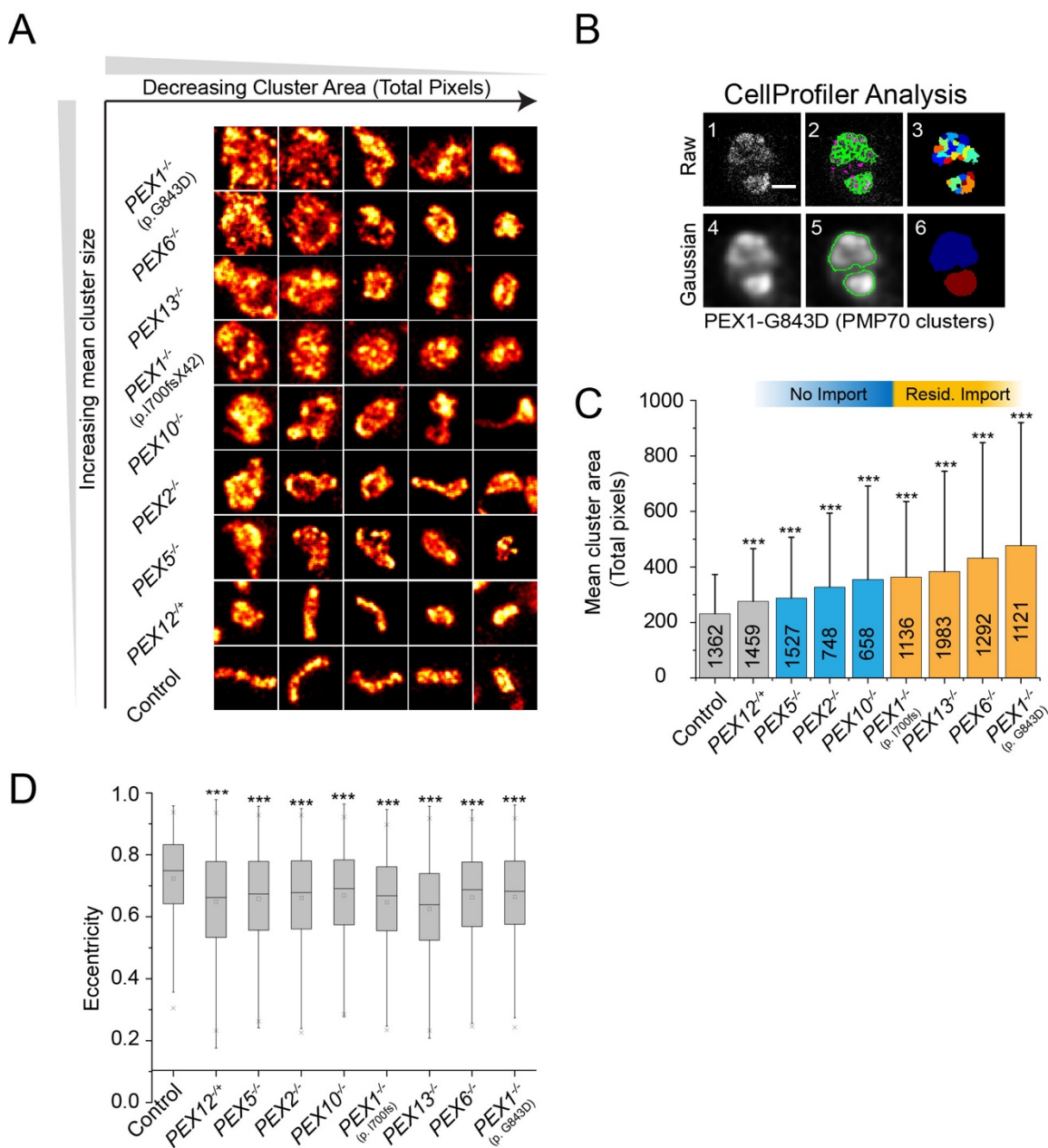


Figure 3.11 ZS ghost peroxisomal remnants STED analysis.

(A) Super-resolution STED tiles (1000 x 1000 nm) of peroxisomal membranes immunostained with anti-PMP70 monoclonal and anti-mouse secondary

antibodies conjugated to Atto594 dye. (B) Raw STED image of ghost clusters from PEX1-G843D ZS cells (1). Segmentation results of the raw image (2). Object map of segmented clusters (3). Gaussian filter image with diameter = 100 nm (4). Segmentation results of Gaussian images (5). Object map of segmented clusters (6). (C) Gaussian analysis with Gaussian diameter of 100 nm, bar graph indicates mean cluster size (Total pixels) \pm Std. Clusters were measured from (n=3) independent experiments, except for *PEX6*^{-/-} (p. S232HfsX15) homozygous and *PEX12*^{-/+} (mosaic) (n=2). The number of ghost clusters measured per condition is indicated on bars and statistics relative to control peroxisome was calculated using two-sample t-test with significance (* $P < 0.01$ or *** $P < 0.0001$ and not significant n.s). (D) Boxplot showing eccentricity calculations of the measured clusters. Statistics using two sample t-test for significance of the mean (*** $P < 0.0001$). STED tile images in (A) were smoothed with an average 3x3 filter. Scale bar 200 nm.

Table 3-1 Patients Summary

PEX gene	Mutation	Catalase	Ghost Size	PMP70 abundance (±SD)	Peroxisome per cell (±SD)	Clinical phenotype reference
PEX1	-/- G843D	CYTO	2.0	1.07 ± 0.39	~ 24%	Mild Ref. [114, 115]
PEX1	-/- I700FS	CYTO	1.57	0.84 ± 0.25	~ 40%	Severe Ref. [116, 117]
PEX6	-/- S232HFS	CYTO	1.86	n.d.	~ 30%	Intermediate Ref. [104]
PEX13	-/- W313G	CYTO	1.65	0.62 ± 0.16	~ 66%	Mild Ref. [104]
PEX10	-/- L272FS	CYTO	1.53	0.47 ± 0.06	~ 23%	Severe (this study)
PEX2	-/- F278FS	CYTO	1.42	0.39 ± 0.02	~ 20%	Severe Ref. [104]
PEX5	-/- Q133X	CYTO	1.25	n.d.	~ 43%	Severe (<i>this study</i>)
PEX12	-/+ 368-370del.TTC	Mosaic	1.19	0.65 ± 0.04	~ 72%	Mild (<i>this study</i>)
Control		PX	1	1	100%	-

n.d. not determined, **CYTO** cytoplasmic, **PX** peroxisomal **Severe:** < 1year, **Intermediate:** > 1 year, **Mild:** > 2 years

STED resolution is essential for accurate ghost size analysis

To address if resolution breakthrough provided by STED microscopy was indispensable to quantify peroxisomal ghost, a confocal-like setting was created by increasing the Gaussian blurring diameter to 250 nm of our STED images, the results changed and the overall cluster size increased, which was related to enlarged PSF and segmentation errors (Fig. 3.12). Therefore, STED microscopy and breaking the diffraction limit are essential to accurately discriminate the ghost structures and thereby provide accurate phenotype distribution.

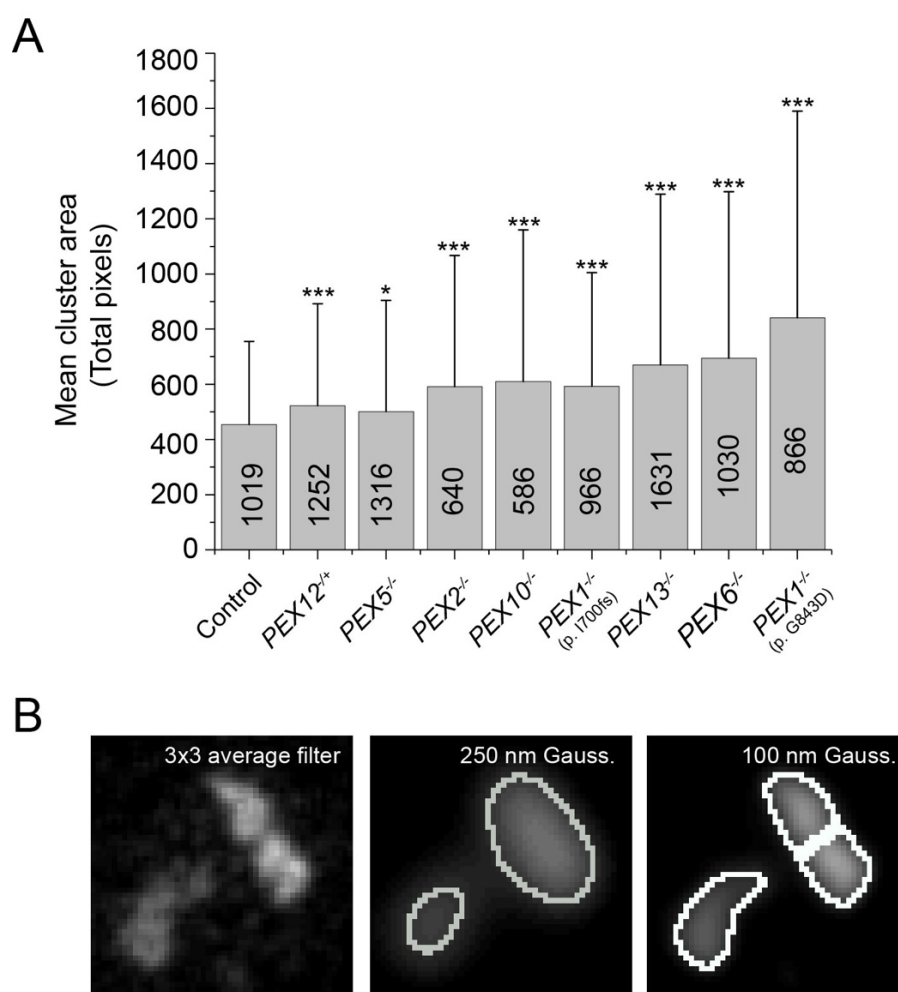


Figure 3.12 Diffraction-limit Gaussian blur and ghost size analysis.

(A) Bar graph of mean ghost cluster size (in total pixels) of STED images blurred with 250 nm Gaussian diameter. Statistics significance (* $P < 0.01$, ** $P < 0.001$,

and *** $P < 0.0001$). (C) Segmentation results of STED images of wild-type peroxisomes using 100 nm Gaussian diameter (left side) and 250 nm Gaussian diameter (right side).

Ghost size in ZSS patients correlates with total PMP70 protein abundance

Previously, differences in PMP70 protein abundance in liver biopsies from ZS patients were reported, which suggested that peroxisomal integral membrane proteins abundance could be critical for the ghost size [47]. To address this question, we carried out a quantification analysis of PMP70 in whole-cell lysates from homozygous ZSS patient fibroblasts of *PEX1*^{-/-} (p.G843D), *PEX1*^{-/-} (p.I700X), *PEX13*^{-/-} (p.W313G), *PEX10*^{-/-} (p.L272X), *PEX2*^{-/-} (p.F278X), and a control cell line by Western blotting. *PEX19*^{-/-} patient cells served as negative control and showed no detectable PMP70 (Fig. 3.13A). The *PEX1*^{-/-}, *PEX13*^{-/-}, and *PEX12*^{-/+} patients showed less reduction in their PMP70 levels, compared to homozygous patients with mutations in RING-family peroxins (Fig. 3.13B). Correlation analysis of ghost size and PMP70 abundance indicated a strong positive relationship between size and PMP70 protein levels (Fig. 3.13C).

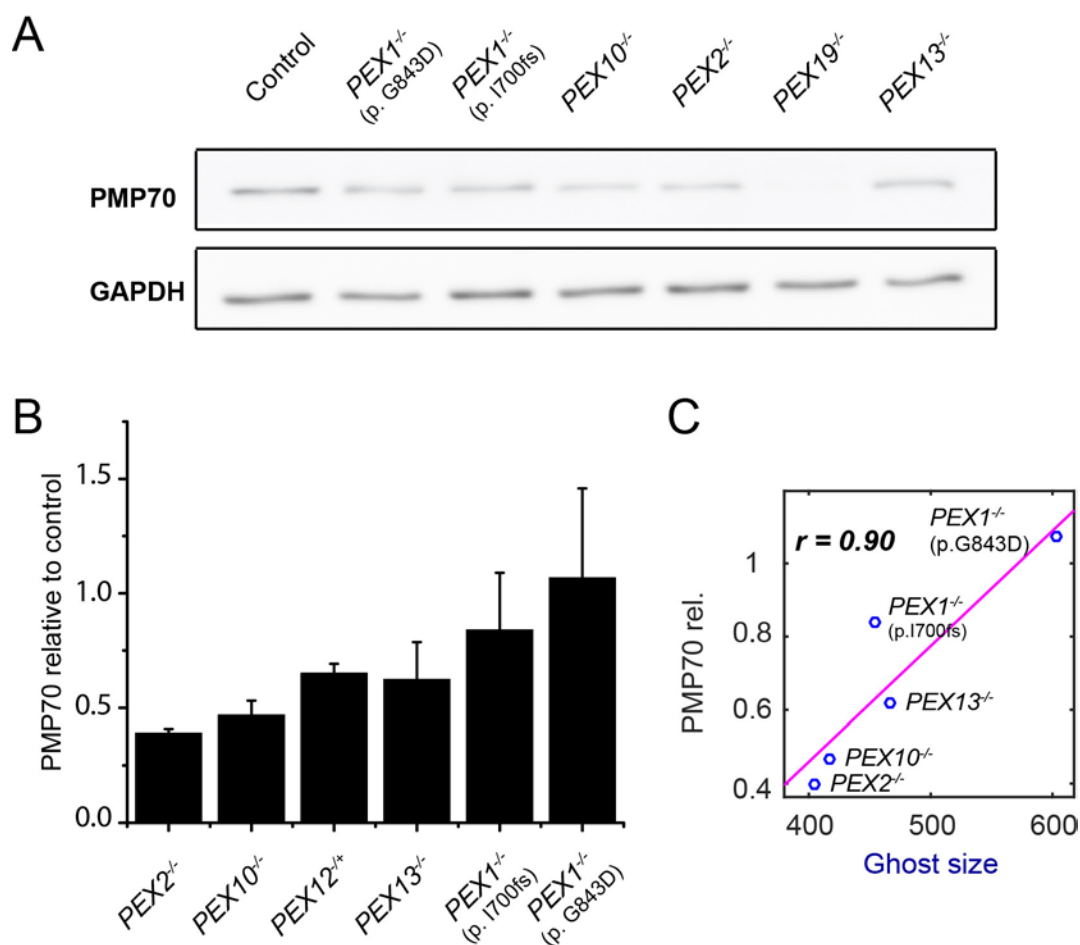


Figure 3.13 PMP70 protein level in ZS patients correlates with ghost size STED phenotype.

(A) Western blot detection of anti-PMP70 from control and HFS fibroblasts. (B) PMP70 quantitation results ($n \geq 3$ per condition). Error bar indicate standard deviation. (C) Pearson correlation of Ghost size and PMP70 protein expression relative to control. Pearson analysis significance was tested using pairwise t-statistics ($P = 0.0543$).

Peroxisome abundance does not correlate with PMP70 abundance

PMP70 abundance might reflect differences in peroxisome number per cell rather than differences in ghost size. To analyze peroxisome ghost numbers in ZSS patients, the number of peroxisomes per cells were quantified by widefield

microscopy and semi-automated imaging analysis. The results of the analysis revealed that the numbers of peroxisomal ghosts were comparable in all ZSS fibroblasts, except for *PEX12*^{-/+} and *PEX5*^{-/-} patients showing slightly less reduction in their ghost abundance (Fig. 3.14A). However, there was no correlation found between ghost number per cell and PMP70 abundance or ghost size (Fig. 3.14B).

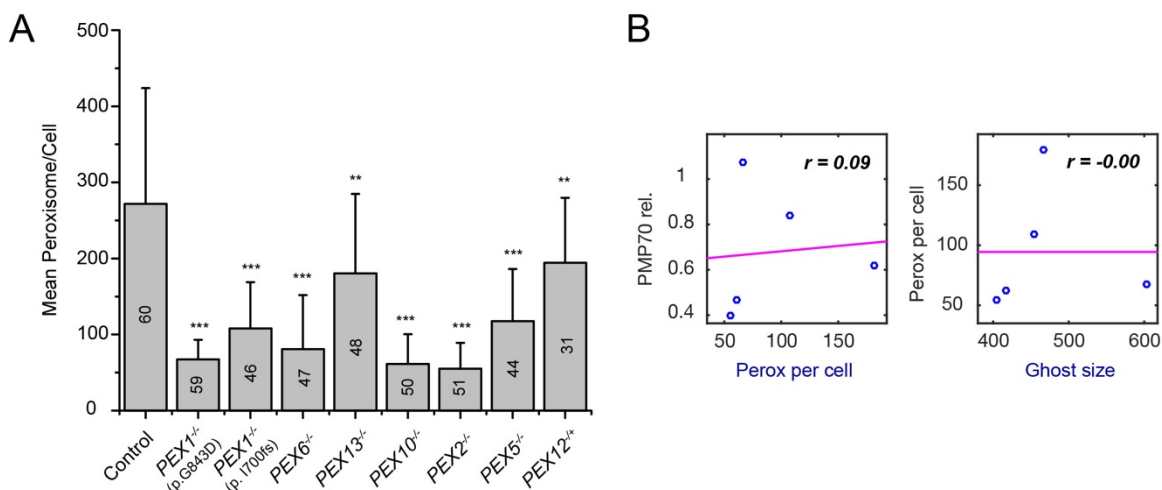


Figure 3.14 Peroxisome ghost quantification.

(A) Bar plot show results of semi-automated analysis of peroxisome ghost. Number indicated on bars indicate the number of cells included in the quantification. Standard deviation was used to determine the error and t-statistics was used to test the significance (** $P < 0.001$ and *** $P < 0.0001$). (B) Pearson correlation plot of PMP70 protein abundance with peroxisome abundance (left) and Peroxisome abundance with ghost size (right). Pearson correlation coefficient (r) is indicated on each graph.

PEX2 interacts with PMP70 *in vivo*

The Western blot analysis showed that *PEX2*^{-/-} patient exhibited the most severe PMP70 abundance phenotype. Previously, our lab has shown that PEX2 overexpression induce PMP70, which proposed a functional link between both proteins [118]. Here, there was no PMP70 upregulation observed under PEX2-

mCitrine overexpression in HeLa cells (Fig 3.15A). However, in this study PEX2 was hypothesized to be an interacting partner of PMP70 thus keeping PMP70 stable at membranes. To test this hypothesis, an immunoprecipitation and pull down PEX2-mCitrine by nanobodies was performed and indeed a PEX2-PMP70 interaction was found (Fig. 3.15B). This novel interaction may explain the significant reduction in PMP70 protein abundance in the *PEX2*^{-/-} ZSS patient's cells. To control for the function of our fusion proteins, overexpressed PEX2-mCitrine and PEX13-mGFP (negative control) in *PEX2* and *PEX13* ZSS fibroblasts, respectively, were able to restore biogenesis as depicted by catalase import in the respective PBD conditions (Fig. 3.15C).

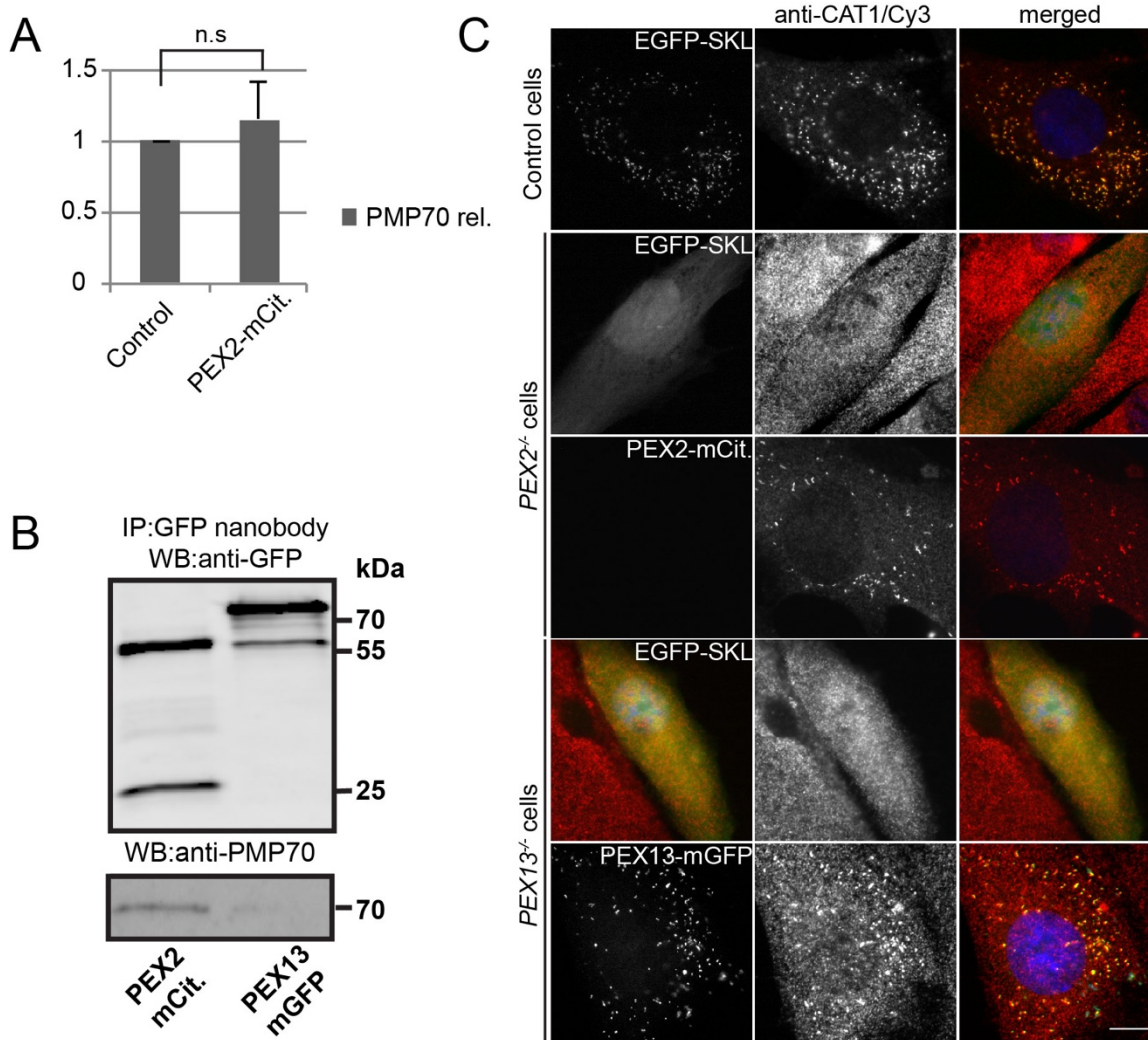


Figure 3.15 PEX2-PMP70 interaction in vivo.

(A) PMP70 Western blot analysis in HeLa cells with PEX2-mCitrine overexpression and without (control). (n = 3, **one way anova, not significant n.s., F-ratio = 4, p = 0.157**) (B) Immunoprecipitation Western blot results of PEX2-mCitrine and PEX13-mGFP with GFP-Trap nanobody (top); co-immunoprecipitation detection of PMP70 (bottom). (C) Control and ZS HSF cells transfected with EGFP-SKL or the respective PEX-Fluorescent Fusion Protein and processed with catalase immunofluorescence.

4. Discussion

In this study, super-resolution STED microscopy was utilized to analyze peroxisome morphology and the localization of different peroxisomal proteins at unprecedented details. In a very recent study, STED microscopy was used to study the peroxisomal compartment and PEX5 distribution under overexpression conditions of GFP-matrix proteins in HSF cells [80]. The authors reported peroxisomes with an average size of ~ 350 nm, which is 2.5 times the size we report here (~100 nm). Earlier EM reports of wildtype peroxisomes under normal conditions revealed an average size of peroxisome of ~100 nm [5]. Therefore, the larger average peroxisomal diameter reported by Galiani et al. as compared to the diameter reported here indicates that overloading peroxisomes with matrix content has a direct effect on peroxisome size. Using STED microscopy and nanobodies, peroxisome diameter in yeast under glucose growth conditions was analyzed and yeast peroxisomes revealed a subdiffraction average diameters of ~ 174 nm under these conditions, which is comparable to earlier EM reports (0.1 μm – 0.2 μm) [12]. In mammalian HeLa cells, the measured average diameter of hyper-tubulated peroxisome while overexpressing PEX11beta was ~ 100 nm, which indicated that PEX11beta does not have any effect on peroxisomal diameter *in vivo*. In contrast, recent *in vitro* studies carried out on proteo-liposomes showed that PEX11beta causes membrane constrictions [33]. Therefore, this study provides a further quantitative evidence that PEX11beta only elongates and does not constrict peroxisomal membrane *in vivo* (Fig. 3.6E), in agreement with the previous qualitative EM observations [119]

Only when peroxisomes were labeled by nanobodies and their subdiffraction architecture were observed by STED microscopy, it was possible to explain the puzzling phenotypes in yeast, associated with deletion or overexpression of a novel peroxisomal protein, PEX35, suggesting that PEX35 controls peroxisome abundance via a vesicular mechanism. This has been supported by other functional experiments (Yofe et al, unpublished). Moreover, peroxisome fission has only been studied by conventional light microscopy and

EM so far [120]. Here we show that the accurate localization of two important peroxisomal fission factors, DLP1 and MFF, by light microscopy, is only achievable with STED resolution. Altogether, this study demonstrates that subdiffraction fluorescence STED microscopy can be effectively used to reveal peroxisome morphology and proteins at a previously unseen level of detail.

4.1. PEX35 a regulator of peroxisome abundance

Peroxisome abundance is regulated by *de novo* formation as well as proliferation and division from preexisting peroxisomes. The process of peroxisome proliferation can be divided into three steps: 1) early membrane vesiculation, 2) elongation, and 3) fission [53]. Arf1 with the coatamer complex and PEX11 are thought to regulate early membrane vesiculation by inducing positive membrane curvature, which is a prerequisite for membrane elongation and polarization [121, 122]. Once membrane curvature is induced, PEX11 functions by promoting membrane elongation and maintaining polarized growth of the membrane [123]. Recently, PEX11 has been found to activate GTP hydrolysis of DLP proteins by showing a selective GAP activity towards them, which suggests an additional role of PEX11 in peroxisome fission [124]. These data led to the hypothesis that PEX11 proteins orchestrate the proliferation process from the beginning to the end [119]; however, it remained unknown how PEX11 could regulate early membrane vesiculation events with Arf1 and its coatamer complex. PEX11 expression does not affect the recruitment of Arf1 to peroxisomes [122]. Brefeldin A, an inhibitor of Arf1-GEF that is required for Arf1-recruitment to the Golgi, did not show any change in peroxisomal Arf1, which suggested that there is another yet unknown Arf1 receptor present on peroxisomal membranes [53]. I contributed to the characterization of the new peroxisomal PEX35 protein that negatively regulates peroxisome abundance and binds to Arf1 (Yofe et al, unpublished). Increased Arf1 recruitment to Golgi has been shown to increase Golgi vesiculation and fission [125]. This is in agreement with the STED microscopy data presented here that show a hyper-vesiculation phenotype of tiny clumped

peroxisomes when overexpressing PEX35, whereas *pex35* deletion shows reduced peroxisome abundance with normal morphology. In STED microscopy, peroxisomes were of slightly bigger size in the knockout compared to the wildtype, but this difference was not statistically significant. The imaging data does not explain why Arf1 is depleted from Golgi membranes in both PEX35 overexpression and deletion (Yofe et al, unpublished). One model is that PEX35 acts as peroxisomal Arf1-GEF receptor; when PEX35 is overexpressed it sequesters Arf1 from the Golgi membranes, thus showing the Arf1 depletion phenotype from Golgi structures and leading to hyper-vesiculated peroxisomes. We hypothesize that when *pex35* is deleted, which does not lead to peroxisomal hyper-vesiculation, an undescribed Arf1 dependent signaling pathway is delivered from peroxisomes to Golgi that leads to Arf1 dissipation and eventually leading to a reduction in Golgi vesiculation. It is not surprising that peroxisomes were found to colocalize with Golgi (Yofe et al, unpublished), and this provides further evidence of such a direct Arf1 dependent pathway that might exist between the two organelles. Another model is that PEX35 acts as a scaffold for a peroxisomal Arf1-GAP, or itself acts as a novel peroxisomal Arf1-GAP protein. In mitochondria, Arf1-GAP overexpression or Arf1-GEF deletion lead to an altered morphology of big and round mitochondria that was found to be clumped small mitochondria (*mito* clusters) (C.-F. Huang, Chen, Tung, Buu, & Lee, 2002), similar to what was observed here in peroxisomes. Deletion of *pex35* (GAP) would then leave a peroxisomal localized Arf1-GEF active, which further accumulates Arf1-GTP on peroxisomal membranes that might lead to an inhibition rather than activation of the Arf1 mediated peroxisome proliferation. Similar in Golgi, *glo3* deletion, a Golgi Arf1-GAP receptor, leads to reduced Golgi numbers per cell, slightly enlarged Golgi and reduced Arf1 puncta were also seen [128]. But how does this second model explain the Arf1 mislocalization from Golgi, in overexpression as well as deletion of PEX35? Pex35 has been shown to interact with Sec7, a Golgi Arf1-GEF. When PEX35 is overexpressed, Sec7 is sequestered from the Golgi membrane and therefore Arf1-GTP accumulation at Golgi membranes is reduced. Whereas in *pex35* deletion the presence of a

peroxisomal Arf1-GEF leads to the sequestration of the Arf1 active pool, and competes with the Arf1 cycle at the Golgi leading to reduced Arf1 puncta, which represent the majority of Golgi membranes.

Current findings suggest Arf1 to be a key factor in balancing cross-talk between peroxisomes and the Golgi. Organelle-coupling does not seem to be a new role of Arf1, as it has been shown to regulate mitochondrial morphology and ER-mitochondrial communication [126]. In the future, the contact-sites and communication between Golgi and peroxisomes will be an interesting field to study in detail. It will improve our understanding of the relationship between peroxisomes and the secretory pathway, in which the Golgi plays a central role. Ultimately, this will improve our understanding of how a cell drives its homeostasis and efficiently couples its metabolic and secretory activities and what goes wrong in various pathologies.

4.2. Mammalian peroxisomal translocon proteins localizations

The process of biogenesis of peroxisomes has been extensively studied, but still fundamental aspects are highly debated and remain to be elucidated. *De novo* formation of peroxisomes has revealed an important role of the endoplasmic reticulum in this process [129–131]. Co-localization microscopy and split-protein assays in yeast have shown RING and docking factors, subcomplexes of the peroxisome translocon, to localize to distinct membrane substructures or vesicles in *pex6* and *pex1* mutant strains, which are referred to as pre-peroxisomal vesicles (PPVs) that derive from ER [20]. Other recent studies did not find differences in the distributions of docking and RING peroxins, even in *pex1* and *pex6* mutants, their results might have been limited by the resolution restraints of widefield colocalization microscopy [22]. Surprisingly, in mammalian cells the colocalization of the RING factors and docking factors has not been investigated. Here, the transient expression of fluorescent-tagged peroxins, small nanobody

labels, and STED microscopy were used to study the colocalization of RING and docking peroxins in mammalian cells. Our data revealed peroxisomal substructures enriched with RING peroxins distinct from those enriched by docking peroxins. Future studies using efficient super-resolution microscopy labels directed against native docking and RING peroxins, will help us to understand the structural and functional arrangement of the peroxisomal factors making up the translocon at greater details. However, our results raise questions about the function of these highly enriched and distinct peroxisomal substructures and their involvement in peroxisome translocon biogenesis and import.

4.3. ZSS ghost phenotype characterization

The description of residual membrane structures ('ghosts') in ZSS patient cells by EM and indirect immunofluorescence microscopy has been important for connecting the genetic defect with the cellular phenotype [44]. We used STED microscopy to further characterize and quantify the morphology the peroxisomal ghost structures in ZSS patients with different *PEX* mutations. We have found that AAA and docking peroxin mutations show larger average peroxisomal ghost sizes, whereas RING-family peroxins mutations revealed compact and smaller peroxisomal ghosts. Residual matrix content has been shown in AAA peroxins and *PEX13* deletions [103, 132, 133]; we therefore hypothesize that the ghost phenotype correlates with residual import. This is in agreement with the different phenotype observed in our two *PEX1*^{-/-} patients, with most severely affected protein (p.I700fsX42) showing smaller peroxisomal ghost size compared to the one with least severe mutation (p.G843D). The *PEX1* G843D^{-/-} allele has been shown to have residually active *PEX1* protein function, which leads to active residual import of matrix proteins compared to the more severe allele I700fs^{-/-} with no active *PEX1* protein function and thus hardly any residual import activity of matrix protein [112]. Also, patients with severe ZSS and mutations affecting

RING factors have abolished peroxisomal import of PTS1 and/or PTS2 targeted proteins [134, 135, 136].

Another factor that might cause variations in the ghost size is differences in the abundance of integral PMPs. Earlier, differences in PMP protein abundance has been observed in various ZSS patients' liver biopsies [44, 136]. Here, we show a positive relationship between PMP70 and ghost size phenotype. Why would less PMP70 lead to smaller ghost size? It is reasonable to think that differences in PMP70 protein abundance could be a result of translocon assembly defects, where some peroxin mutations might interfere with the overall integrity of PMPs at peroxisomal membranes. This is supported by the severely reduced PMP70 abundance in the *PEX2*^{-/-} patient and the identification of a PEX2-PMP70 interaction. At the same time, integral PMPs might have a direct effect on peroxisomal membrane formation. To prove this, depletion of various integral PMPs in fission defect peroxisomes should show a similar phenotype correlation between peroxisome size and PMP abundance. Experiments on different organelles have revealed similar effects of reduced membrane protein abundance on organelle size and membrane ultrastructure [137, 138]. Finally, variabilities in the ZSS ghost's phenotype may be a combination of residual import activity, local PMP stability, and further unknown factors that associate with the pathological state of ZSS disorders. In the future, to accurately identify the protein content of peroxisomal ghost vesicles and their respective size we would have to measure the copy number of ghosts, the amount of associated proteins and the size of ghosts simultaneously on a single molecule and a single vesicle basis, which could be achieved by peroxisome vesicle separation and proteomics on purified peroxisomal ghosts.

In conclusion, STED resolution is critically required for accurate characterization and quantification of the ghost morphology in ZSS patient cells since emulating confocal images from the STED images by Gaussian blurring revealed that it is not possible to differentiate various ZSS phenotypes under

confocal resolution. This work further shows that not only residual import function correlates with the prognosis of ZSS patients, but also a sub-diffraction morphological ghost phenotype. In future, the sub-diffraction morphological analysis of the ghost phenotype of ZSS patients could be implemented in the clinical practice and complement other prognostic and diagnostic tests for peroxisomal disorders. This will lead to a better understanding of the molecular pathology of ZSS and path the way to establish therapeutic approaches.

5. Conclusion

The work described here shows how super-resolution microscopy can be used in addition to other techniques to reveal new information about peroxisomal proteins and the morphology of peroxisomes in yeast and human cells. Clinically significant, we have found that the cellular peroxisomal ghost phenotype in the cells of ZSS patients correlates with the molecular and clinical severity of the disease. Finally, the experiments and analysis presented in this thesis provide a starting point for future studies on the application of super-resolution microscopy to study peroxisome biology.

6. Appendix

6.1. Matlab Script codes

%% Calculate diameter of peroxisome automatically from all selected CSV reads

```
[Filename,PathName]=uigetfile({'*.csv*'},...
'Multiselect', 'on');
cd(PathName);
for k = 1:length(Filename)
    file = fullfile(PathName, Filename{k});
    fid= fopen(file, 'r');
    fgets(fid);
    if isequal(fid,0)
        disp('User selected Cancel')
    else
        readData = textscan(fid,'%f %f','HeaderLines',1,'Delimiter',' ');
        xData = readData{1,1}(:,1);
        yData = readData{1,2}(:,1);
        f1 = fit(xData*1000,yData,'gauss2')
        coeffvalues(f1)
        a = ans(:,2)
        b = ans(:,5)
        diameter(k) = a-b
        diameter_positive = abs(diameter);
```

```
boxplot(diameter_positive)

end

    end

        B = transpose(diameter_positive)
        csvwrite('diameter_results.csv',B);

%% Calculate FWHM automatically from all selected CSV reads

[Filename,PathName]=uigetfile({'*.csv*'},...
    'Multiselect', 'on');

    cd(PathName);

    for k = 1:length(Filename)

        file = fullfile(PathName, Filename{k});

        fid= fopen(file, 'r');

        fgets(fid);

    if isequal(fid,0)

        disp('User selected Cancel')

    else

        readData = textscan(fid,'%f %f','HeaderLines',1,'Delimiter',' ');

        xData = readData{1,1}(:,1);

        yData = readData{1,2}(:,1);

        f1 = fit(xData*1000,yData,'gauss1')

        coeffvalues(f1)

        a = ans(:,3)

        FWMH(k) = a

        FWMH_positive = abs(FWMH*1.63);
```

```
boxplot(FWMH_positive)
end
end
B = transpose(FWMH_positive)
csvwrite('FWMH_results.csv',B);
```

7. Bibliography

1. De Duve C, Baudhuin P (1966) Peroxisomes (microbodies and related particles). *Physiol Rev* 46:323–57.
2. Smith JJ, Aitchison JD (2013) Peroxisomes take shape. *Nat Rev Mol Cell Biol* 14:803–17. doi: 10.1038/nrm3700
3. Liu F, Ng SK, Lu Y, et al (2008) Making two organelles from one: Woronin body biogenesis by peroxisomal protein sorting. *J Cell Biol* 180:325–339. doi: 10.1083/jcb.200705049
4. Parsons M, Furuya T, Pal S, Kessler P (2001) Biogenesis and function of peroxisomes and glycosomes. *Mol Biochem Parasitol* 115:19–28. doi: doi:10.1016/S0166-6851(01)00261-4
5. Fahimi D, Sies H (1987) *Peroxisomes in Biology and Medicine*. Springer Proc Life Sci XVIII:164. doi: 10.1007/978-3-642-71325-5
6. Heintzmann R, Ficz G (2006) Breaking the resolution limit in light microscopy. *Briefings Funct Genomics Proteomics* 5:289–301. doi: 10.1093/bfgp/ell036
7. Titorenko VI, Rachubinski RA (2001) The life cycle of the peroxisome. *Nat Rev Mol Cell Biol* 2:357–68. doi: 10.1038/35073063
8. Platta HW, Erdmann R (2007) The peroxisomal protein import machinery. *FEBS Lett* 581:2811–2819. doi: 10.1016/j.febslet.2007.04.001
9. Brown AI, Kim PK, Rutenberg AD (2014) PEX5 and ubiquitin dynamics on mammalian peroxisome membranes. *PLoS Comput Biol* 10:e1003426. doi: 10.1371/journal.pcbi.1003426
10. Subramani S (1996) Protein Translocation into Peroxisomes. *J Biol Chem* 271:32483–32486. doi: 10.1074/jbc.271.51.32483

11. Agrawal G, Subramani S (2015) De novo peroxisome biogenesis: Evolving concepts and conundrums. *Biochim Biophys Acta*. doi: 10.1016/j.bbamcr.2015.09.014
12. Purdue PE, Lazarow PB (2001) Peroxisome Biogenesis. *Annu Rev Cell Dev Biol* 17:701–52. doi: 10.1146/annurev.cellbio.17.1.701
13. Distel B, Erdmann R, Gould SJ, et al (1996) A unified nomenclature for peroxisome biogenesis factors. *J Cell Biol* 135:1–3. doi: 10.1083/jcb.135.1.1
14. Mayerhofer PU, Bañó-Polo M, Mingarro I, Johnson AE (2016) Human Peroxin PEX3 Is Co-translationally Integrated into the ER and Exits the ER in Budding Vesicles. *Traffic* 17:117–130. doi: 10.1111/tra.12350
15. Thoms S, Harms I, Kalies K-U, Gärtner J (2012) Peroxisome formation requires the endoplasmic reticulum channel protein Sec61. *Traffic* 13:599–609. doi: 10.1111/j.1600-0854.2011.01324.x
16. Fang Y, Morrell JC, Jones JM, Gould SJ (2004) PEX3 functions as a PEX19 docking factor in the import of class I peroxisomal membrane proteins. *J Cell Biol* 164:863–75. doi: 10.1083/jcb.200311131
17. Van Ael E, Fransen M (2006) Targeting signals in peroxisomal membrane proteins. *Biochim Biophys Acta - Mol Cell Res* 1763:1629–1638. doi: 10.1016/j.bbamcr.2006.08.020
18. Fujiki Y, Okumoto K, Mukai S, et al (2014) Peroxisome biogenesis in mammalian cells. *Front Physiol* 5:307. doi: 10.3389/fphys.2014.00307
19. Sakaue H, Iwashita S, Yamashita Y, et al (2015) The N-terminal motif of PMP70 suppresses cotranslational targeting to the endoplasmic reticulum. *J Biochem* 159:539–51. doi: 10.1093/jb/mvv132
20. van der Zand A, Gent J, Braakman I, Tabak HF (2012) Biochemically distinct vesicles from the endoplasmic reticulum fuse to form peroxisomes. *Cell* 149:397–409. doi: 10.1016/j.cell.2012.01.054

21. Girzalsky W, Saffian D, Erdmann R (2010) Peroxisomal protein translocation. *Biochim Biophys Acta* 1803:724–31. doi: 10.1016/j.bbamcr.2010.01.002
22. Knoops K, de Boer R, Kram A, van der Klei IJ (2015) Yeast pex1 cells contain peroxisomal ghosts that import matrix proteins upon reintroduction of Pex1. *J Cell Biol* 211:955–62. doi: 10.1083/jcb.201506059
23. Schrader M, Bonekamp NA, Islinger M (2012) Fission and proliferation of peroxisomes. *Biochim Biophys Acta* 1822:1343–57. doi: 10.1016/j.bbadis.2011.12.014
24. Latruffe N, Vamecq J (1997) Peroxisome proliferators and peroxisome proliferator activated receptors (PPARs) as regulators of lipid metabolism. *Biochimie* 79:81–94. doi: 10.1016/S0300-9084(97)81496-4
25. Karpichev I V, Small GM (1998) Global regulatory functions of Oaf1p and Pip2p (Oaf2p), transcription factors that regulate genes encoding peroxisomal proteins in *Saccharomyces cerevisiae*. *Mol Cell Biol* 18:6560–70.
26. Sirtori C, Fumagalli R, Paoletti R (1973) Hypolipidemic drugs. *Adv Exp Med Biol* 38:171–98.
27. Reddy JK, Krishnakantha TP (1975) Hepatic peroxisome proliferation: induction by two novel compounds structurally unrelated to clofibrate. *Science* 190:787–9. doi: DOI: 10.1126/science.1198095
28. Erdmann R, Blobel G (1995) Giant peroxisomes in oleic acid-induced *Saccharomyces cerevisiae* lacking the peroxisomal membrane protein Pmp27p. *J Cell Biol* 128:509–23. doi: doi:10.1083/jcb.128.4.509
29. Lockshon D, Surface LE, Kerr EO, et al (2007) The sensitivity of yeast mutants to oleic acid implicates the peroxisome and other processes in membrane function. *Genetics* 175:77–91. doi: 10.1534/genetics.106.064428

30. Thoms S, Erdmann R (2005) Dynamin-related proteins and Pex11 proteins in peroxisome division and proliferation. *FEBS J* 272:5169–81. doi: 10.1111/j.1742-4658.2005.04939.x
31. Koch J, Pranjic K, Huber A, et al (2010) PEX11 family members are membrane elongation factors that coordinate peroxisome proliferation and maintenance. *J Cell Sci* 123:3389–400. doi: 10.1242/jcs.064907
32. Schrader M, Reuber BE, Morrell JC, et al (1998) Expression of PEX11beta mediates peroxisome proliferation in the absence of extracellular stimuli. *J Biol Chem* 273:29607–14.
33. Yoshida Y, Niwa H, Honsho M, et al (2015) Pex11 mediates peroxisomal proliferation by promoting deformation of the lipid membrane. *Biol Open* 4:710–21. doi: 10.1242/bio.201410801
34. Koch A, Thiemann M, Grabenbauer M, et al (2003) Dynamin-like protein 1 is involved in peroxisomal fission. *J Biol Chem* 278:8597–605. doi: 10.1074/jbc.M211761200
35. Gandre-Babbe S, van der Blik AM (2008) The novel tail-anchored membrane protein Mff controls mitochondrial and peroxisomal fission in mammalian cells. *Mol Biol Cell* 19:2402–12. doi: 10.1091/mbc.E07-12-1287
36. Koch J, Brocard C (2012) PEX11 proteins attract Mff and human Fis1 to coordinate peroxisomal fission. *J Cell Sci* 125:3813–26. doi: 10.1242/jcs.102178
37. Rosenbloom AB, Lee S-H, To M, et al (2014) Optimized two-color super resolution imaging of Drp1 during mitochondrial fission with a slow-switching Dronpa variant. *Proc Natl Acad Sci U S A* 111:13093–8. doi: 10.1073/pnas.1320044111

38. Weller S, Gould SJ, Valle D (2003) Peroxisome Biogenesis Disorders. *Annu Rev Genomics Hum Genet* 4:165-211. doi: 10.1146/annurev.genom.4.070802.110424
39. Steinberg SJ, Dodt G, Raymond G V., et al (2006) Peroxisome biogenesis disorders. *Biochim Biophys Acta - Mol Cell Res* 1763:1733–1748. doi: 10.1016/j.bbamcr.2006.09.010
40. Krause C, Rosewich H, Gärtner J (2009) Rational diagnostic strategy for Zellweger syndrome spectrum patients. *Eur J Hum Genet* 17:741–8. doi: 10.1038/ejhg.2008.252
41. Rosewich H, Waterham H, Poll-The BT, et al (2015) Clinical utility gene card for: Zellweger syndrome spectrum. *Eur J Hum Genet*. doi: 10.1038/ejhg.2014.250
42. Ratbi I, Falkenberg KD, Sommen M, et al (2015) Heimler Syndrome Is Caused by Hypomorphic Mutations in the Peroxisome-Biogenesis Genes PEX1 and PEX6. *Am J Hum Genet* 97:535–45. doi: 10.1016/j.ajhg.2015.08.011
43. Santos MJ, Imanaka T, Shio H, et al (1988) Peroxisomal membrane ghosts in Zellweger syndrome--aberrant organelle assembly. *Science* 239:1536–8. doi: DOI: 10.1126/science.3281254
44. Santos MJ, Hoefler S, Moser AB, et al (1992) Peroxisome assembly mutations in humans: structural heterogeneity in Zellweger syndrome. *J Cell Physiol* 151:103–12. doi: 10.1002/jcp.1041510115
45. Koek A, Komori M, Veenhuis M, van der Klei IJ (2007) A comparative study of peroxisomal structures in *Hansenula polymorpha* pex mutants. *FEMS Yeast Res* 7:1126–33. doi: 10.1111/j.1567-1364.2007.00261.x
46. Kim PK, Hetteema EH (2015) Multiple pathways for protein transport to peroxisomes. *J Mol Biol* 427:1176–90. doi: 10.1016/j.jmb.2015.02.005

47. Small GM, Santos MJ, Imanaka T, et al (1988) Peroxisomal integral membrane proteins in livers of patients with Zellweger syndrome, infantile Refsum's disease and X-linked adrenoleukodystrophy. *J Inherit Metab Dis* 11:358–71. doi: 10.1007/BF01800425
48. Nunnari J, Walter P (1996) Regulation of Organelle Biogenesis. *Cell* 84:389–394. doi: 10.1016/S0092-8674(00)81283-0
49. Botstein D, Chervitz SA, Cherry JM (1997) Yeast as a model organism. *Science* 277:1259–60. doi: 10.1126/science.277.5330.1259
50. Duina AA, Miller ME, Keeney JB (2014) Budding yeast for budding geneticists: a primer on the *Saccharomyces cerevisiae* model system. *Genetics* 197:33–48. doi: 10.1534/genetics.114.163188
51. Tower RJ, Fagarasanu A, Aitchison JD, Rachubinski RA (2011) The peroxin Pex34p functions with the Pex11 family of peroxisomal divisional proteins to regulate the peroxisome population in yeast. *Mol Biol Cell* 22:1727–38. doi: 10.1091/mbc.E11-01-0084
52. Hoepfner D, van den Berg M, Philippsen P, et al (2001) A role for Vps1p, actin, and the Myo2p motor in peroxisome abundance and inheritance in *Saccharomyces cerevisiae*. *J Cell Biol* 155:979–90. doi: 10.1083/jcb.200107028
53. Lay D, Gorgas K, Just WW (2006) Peroxisome biogenesis: where Arf and coatomer might be involved. *Biochim Biophys Acta* 1763:1678–87. doi: 10.1016/j.bbamcr.2006.08.036
54. Veenhuis M, Mateblowski M, Kunau WH, Harder W (1987) Proliferation of microbodies in *Saccharomyces cerevisiae*. *Yeast* 3:77–84. doi: 10.1002/yea.320030204
55. Erdmann R, Veenhuis M, Mertens D, Kunau WH (1989) Isolation of peroxisome-deficient mutants of *Saccharomyces cerevisiae*. *Proc Natl Acad Sci U S A* 86:5419–23.

56. Desfougères T, Ferreira T, Bergès T, et al (2008) SFH2 regulates fatty acid synthase activity in the yeast *Saccharomyces cerevisiae* and is critical to prevent saturated fatty acid accumulation in response to haem and oleic acid depletion. *Biochem J* 409:299–309. doi: 10.1042/BJ20071028
57. Hiltunen JK, Mursula AM, Rottensteiner H, et al (2003) The biochemistry of peroxisomal beta-oxidation in the yeast *Saccharomyces cerevisiae*. *FEMS Microbiol Rev* 27:35–64. doi: 10.1016/s0168-6445(03)00017-2
58. Wolinski H, Petrovic U, Mattiazzi M, et al (2009) Imaging-based live cell yeast screen identifies novel factors involved in peroxisome assembly. *J Proteome Res* 8:20–7. doi: 10.1021/pr800782n
59. Cohen Y, Klug YA, Dimitrov L, et al (2014) Peroxisomes are juxtaposed to strategic sites on mitochondria. *Mol Biosyst* 10:1742–8. doi: 10.1039/c4mb00001c
60. Yofe I, Weill U, Meurer M, et al (2016) One library to make them all: streamlining the creation of yeast libraries via a SWAp-Tag strategy. *Nat Methods*. doi: 10.1038/nmeth.3795
61. Cohen Y, Schuldiner M (2011) Advanced methods for high-throughput microscopy screening of genetically modified yeast libraries. *Methods Mol Biol* 781:127–59. doi: 10.1007/978-1-61779-276-2_8
62. Smolyaninov II (2008) Optical microscopy beyond the diffraction limit. *HFSP J* 2:129–31. doi: 10.2976/1.2912559
63. Lauterbach MA (2012) Finding, defining and breaking the diffraction barrier in microscopy -- a historical perspective. *Opt Nanoscopy* 1:1–8. doi: 10.1186/2192-2853-1-8
64. Möckl L, Lamb DC, Bräuchle C (2014) Super-resolved Fluorescence Microscopy: Nobel Prize in Chemistry 2014 for Eric Betzig, Stefan Hell, and William E. Moerner. *Angew Chemie Int Ed* 53:13972–13977. doi: 10.1002/anie.201410265

65. Hell SW (2007) Far-field optical nanoscopy. *Science* 316:365–398. doi: 10.1126/science.1137395
66. Hell SW, Wichmann J (1994) Breaking the diffraction resolution limit by stimulated emission: stimulated-emission-depletion fluorescence microscopy. *Opt Lett* 19:780–2.
67. Moerner WE, Dickson RM, Cubitt AB, Tsien RY (1997) On/off blinking and switching behaviour of single molecules of green fluorescent protein. *Nature* 388:355–358. doi: 10.1038/41048
68. Huang B, Bates M, Zhuang X (2009) Super-resolution fluorescence microscopy. *Annu Rev Biochem* 78:993–1016. doi: 10.1146/annurev.biochem.77.061906.092014
69. Whelan DR, Bell TDM (2015) Super-Resolution Single-Molecule Localization Microscopy: Tricks of the Trade. *J Phys Chem Lett* 6:374–382. doi: 10.1021/jz5019702
70. Müller T, Schumann C, Kraegeloh A (2012) STED microscopy and its applications: new insights into cellular processes on the nanoscale. *Chemphyschem* 13:1986–2000. doi: 10.1002/cphc.201100986
71. Harke B, Bianchini P, Vicidomini G, et al (2013) Stimulated Emission Depletion (STED) Microscopy. In: *Encycl. Biophys.* Springer Berlin Heidelberg, Berlin, Heidelberg, pp 2470–2475
72. Hell SW (2007) Far-field optical nanoscopy. *Science* 316:1153–8. doi: 10.1126/science.1137395
73. Eggeling C, Widengren J, Rigler R, Seidel CAM (1998) Photobleaching of Fluorescent Dyes under Conditions Used for Single-Molecule Detection: Evidence of Two-Step Photolysis. *Anal Chem* 70:2651–2659. doi: 10.1021/ac980027p

74. Vicidomini G, Schönle A, Ta H, et al (2013) STED nanoscopy with time-gated detection: theoretical and experimental aspects. *PLoS One* 8:e54421. doi: 10.1371/journal.pone.0054421
75. Rittweger E, Han KY, Irvine SE, et al (2009) STED microscopy reveals crystal colour centres with nanometric resolution. *Nat Photonics* 3:144–147. doi: 10.1038/nphoton.2009.2
76. Laporte G, Psaltis D (2016) STED imaging of green fluorescent nanodiamonds containing nitrogen-vacancy-nitrogen centers. *Biomed Opt Express* 7:34–44. doi: 10.1364/BOE.7.000034
77. Göttfert F, Wurm CA, Mueller V, et al (2013) Coaligned dual-channel STED nanoscopy and molecular diffusion analysis at 20 nm resolution. *Biophys J* 105:L01-3. doi: 10.1016/j.bpj.2013.05.029
78. Klar TA, Jakobs S, Dyba M, et al (2000) Fluorescence microscopy with diffraction resolution barrier broken by stimulated emission. *Proc Natl Acad Sci* 97:8206–8210. doi: 10.1073/pnas.97.15.8206
79. Jakobs S, Wurm CA (2014) Super-resolution microscopy of mitochondria. *Curr Opin Chem Biol* 20:9–15. doi: 10.1016/j.cbpa.2014.03.019
80. Galiani S, Waithe D, Reglinski K, et al (2016) Super resolution microscopy reveals compartmentalization of peroxisomal membrane proteins. *J Biol Chem* jbc.M116.734038. doi: 10.1074/jbc.M116.734038
81. Willig KI, Rizzoli SO, Westphal V, et al (2006) STED microscopy reveals that synaptotagmin remains clustered after synaptic vesicle exocytosis. *Nature* 440:935–939. doi: 10.1038/nature04592
82. Fernández-Suárez M, Ting AY (2008) Fluorescent probes for super-resolution imaging in living cells. *Nat Rev Mol Cell Biol* 9:929–943. doi: 10.1038/nrm2531

83. Yang Z, Sharma A, Qi J, et al (2016) Super-resolution fluorescent materials: an insight into design and bioimaging applications. *Chem Soc Rev*. doi: 10.1039/C5CS00875A
84. MacDonald L, Baldini G, Storrie B (2015) Does super-resolution fluorescence microscopy obsolete previous microscopic approaches to protein co-localization? *Methods Mol Biol* 1270:255–75. doi: 10.1007/978-1-4939-2309-0_19
85. Pleiner T, Bates M, Trakhanov S, et al (2015) Nanobodies: site-specific labeling for super-resolution imaging, rapid epitope-mapping and native protein complex isolation. *Elife* 4:e11349. doi: 10.7554/eLife.11349
86. Platonova E, Winterflood CM, Junemann A, et al (2015) Single-molecule microscopy of molecules tagged with GFP or RFP derivatives in mammalian cells using nanobody binders. *Methods* 88:89–97. doi: 10.1016/j.ymeth.2015.06.018
87. Ries J, Kaplan C, Platonova E, et al (2012) A simple, versatile method for GFP-based super-resolution microscopy via nanobodies. *Nat Methods* 9:582–584. doi: 10.1038/nmeth.1991
88. Opazo F, Levy M, Byrom M, et al (2012) Aptamers as potential tools for super-resolution microscopy. *Nat Methods* 9:938–939. doi: 10.1038/nmeth.2179
89. Chen S-C, Zhao T, Gordon GJ, Murphy RF (2007) Automated image analysis of protein localization in budding yeast. *Bioinformatics* 23:i66-71. doi: 10.1093/bioinformatics/btm206
90. Wollman R, Stuurman N (2007) High throughput microscopy: from raw images to discoveries. *J Cell Sci* 120:3715–22. doi: 10.1242/jcs.013623

91. Löschberger A, van de Linde S, Dabauvalle M-C, et al (2012) Super-resolution imaging visualizes the eightfold symmetry of gp210 proteins around the nuclear pore complex and resolves the central channel with nanometer resolution. *J Cell Sci* 125:570–5. doi: 10.1242/jcs.098822
92. Lau L, Lee YL, Sahl SJ, et al (2012) STED microscopy with optimized labeling density reveals 9-fold arrangement of a centriole protein. *Biophys J* 102:2926–35. doi: 10.1016/j.bpj.2012.05.015
93. Pagoon S V, Cordoba S-P, Owen DM, et al (2013) Superresolution microscopy reveals nanometer-scale reorganization of inhibitory natural killer cell receptors upon activation of NKG2D. *Sci Signal* 6:ra62. doi: 10.1126/scisignal.2003947
94. Chen K-CJ, Yang G, Kovacevic J (2014) Spatial density estimation based segmentation of super-resolution localization microscopy images. In: 2014 IEEE Int. Conf. Image Process. IEEE, pp 867–871
95. Klotzsch E, Smorodchenko A, Löfler L, et al (2015) Superresolution microscopy reveals spatial separation of UCP4 and F0F1-ATP synthase in neuronal mitochondria. *Proc Natl Acad Sci U S A* 112:130–5. doi: 10.1073/pnas.1415261112
96. Wählby C, Sintorn I-M, Erlandsson F, et al (2004) Combining intensity, edge and shape information for 2D and 3D segmentation of cell nuclei in tissue sections. *J Microsc* 215:67–76. doi: 10.1111/j.0022-2720.2004.01338.x
97. Carpenter AE, Jones TR, Lamprecht MR, et al (2006) CellProfiler: image analysis software for identifying and quantifying cell phenotypes. *Genome Biol* 7:R100. doi: 10.1186/gb-2006-7-10-r100
98. Soliman K (2015) CellProfiler: Novel Automated Image Segmentation Procedure for Super-Resolution Microscopy. *Biol Proced Online* 17:11. doi: 10.1186/s12575-015-0023-9

99. Taxis C, Knop M (2006) System of centromeric, episomal, and integrative vectors based on drug resistance markers for *Saccharomyces cerevisiae*. *Biotechniques* 40:73–8.
100. Janke C, Magiera MM, Rathfelder N, et al (2004) A versatile toolbox for PCR-based tagging of yeast genes: new fluorescent proteins, more markers and promoter substitution cassettes. *Yeast* 21:947–62. doi: 10.1002/yea.1142
101. Kaplan C, Ewers H (2015) Optimized sample preparation for single-molecule localization-based superresolution microscopy in yeast. *Nat Protoc* 10:1007–1021. doi: 10.1038/nprot.2015.060
102. Canelas AB, ten Pierick A, Ras C, et al (2009) Quantitative Evaluation of Intracellular Metabolite Extraction Techniques for Yeast Metabolomics. *Anal Chem* 81:7379–7389. doi: 10.1021/ac900999t
103. Krause C, Rosewich H, Woehler A, Gärtner J (2013) Functional analysis of PEX13 mutation in a Zellweger syndrome spectrum patient reveals novel homooligomerization of PEX13 and its role in human peroxisome biogenesis. *Hum Mol Genet* 22:3844–57. doi: 10.1093/hmg/ddt238
104. Krause C, Rosewich H, Thanos M, Gärtner J (2006) Identification of novel mutations in PEX2, PEX6, PEX10, PEX12, and PEX13 in Zellweger spectrum patients. *Hum Mutat* 27:1157. doi: 10.1002/humu.9462
105. Mahmood T, Yang P-C (2012) Western blot: technique, theory, and trouble shooting. *N Am J Med Sci* 4:429–34. doi: 10.4103/1947-2714.100998
106. Wright K (1989) Antibodies a Laboratory Manual. *Biochem Educ* 17:220. doi: 10.1016/0307-4412(89)90165-9
107. Kiyatkin A, Aksamitiene E (2009) Multistrip western blotting to increase quantitative data output. *Methods Mol Biol* 536:149–61. doi: 10.1007/978-1-59745-542-8_17

108. Breitling R, Sharif O, Hartman ML, Krisans SK (2002) Loss of compartmentalization causes misregulation of lysine biosynthesis in peroxisome-deficient yeast cells. *Eukaryot Cell* 1:978–86.
109. Noguchi T (1987) *Amino Acid Metabolism in Animal Peroxisomes*. Springer Berlin Heidelberg, pp 234–243
110. Schrader M, Bonekamp NA, Islinger M (2012) Fission and proliferation of peroxisomes. *Biochim Biophys Acta - Mol Basis Dis* 1822:1343–1357. doi: 10.1016/j.bbadis.2011.12.014
111. Yoon Y, Pitts KR, McNiven MA (2001) Mammalian dynamin-like protein DLP1 tubulates membranes. *Mol Biol Cell* 12:2894–905.
112. Walter C, Gootjes J, Mooijer PA, et al (2001) Disorders of Peroxisome Biogenesis Due to Mutations in PEX1: Phenotypes and PEX1 Protein Levels. *Am J Hum Genet* 69:35–48. doi: <http://dx.doi.org/10.1086/321265>
113. Nguyen T, Bjorkman J, Paton BC, Crane DI (2006) Failure of microtubule-mediated peroxisome division and trafficking in disorders with reduced peroxisome abundance. *J Cell Sci* 119:636–45. doi: 10.1242/jcs.02776
114. Rosewich H, Ohlenbusch A, Gärtner J (2005) Genetic and clinical aspects of Zellweger spectrum patients with PEX1 mutations. *J Med Genet* 42:e58. doi: 10.1136/jmg.2005.033324
115. Ebberink MS, Mooijer PAW, Gootjes J, et al (2011) Genetic classification and mutational spectrum of more than 600 patients with a Zellweger syndrome spectrum disorder. *Hum Mutat* 32:59–69. doi: 10.1002/humu.21388
116. Rosewich H (2005) Genetic and clinical aspects of Zellweger spectrum patients with PEX1 mutations. *J Med Genet* 42:e58–e58. doi: 10.1136/jmg.2005.033324

117. Waterham HR, Ebberink MS (2012) Genetics and molecular basis of human peroxisome biogenesis disorders. *Biochim Biophys Acta - Mol Basis Dis* 1822:1430–1441. doi: 10.1016/j.bbadis.2012.04.006
118. Gärtner J, Brosius U, Obie C, et al (1998) Restoration of PEX2 peroxisome assembly defects by overexpression of PMP70. *Eur J Cell Biol* 76:237–45. doi: 10.1016/S0171-9335(98)80001-0
119. Koch J, Pranjic K, Huber A, et al (2010) PEX11 family members are membrane elongation factors that coordinate peroxisome proliferation and maintenance. *J Cell Sci* 123:3389–400. doi: 10.1242/jcs.064907
120. Itoyama A, Michiyuki S, Honsho M, et al (2013) Mff functions with Pex11p β and DLP1 in peroxisomal fission. *Biol Open* 2:998–1006. doi: 10.1242/bio.20135298
121. Beck R, Sun Z, Adolf F, et al (2008) Membrane curvature induced by Arf1-GTP is essential for vesicle formation. *Proc Natl Acad Sci* 105:11731–11736. doi: 10.1073/pnas.0805182105
122. Anton M, Passreiter M, Lay D, et al (2000) ARF- and coatomer-mediated peroxisomal vesiculation. *Cell Biochem Biophys* 32 Spring:27–36.
123. Johannes Koch CB (2011) Membrane elongation factors in organelle maintenance: the case of peroxisome proliferation. *Biomol Concepts* 2:353.
124. Williams C, Opalinski L, Landgraf C, et al (2015) The membrane remodeling protein Pex11p activates the GTPase Dnm1p during peroxisomal fission. *Proc Natl Acad Sci U S A* 112:6377–82. doi: 10.1073/pnas.1418736112
125. Kuai J, Boman AL, Arnold RS, et al (2000) Effects of Activated ADP-ribosylation Factors on Golgi Morphology Require neither Activation of Phospholipase D1 nor Recruitment of Coatomer. *J Biol Chem* 275:4022–4032. doi: 10.1074/jbc.275.6.4022

126. Ackema KB, Hench J, Böckler S, et al (2014) The small GTPase Arf1 modulates mitochondrial morphology and function. *EMBO J* 33:2659–75. doi: 10.15252/emj.201489039
127. Huang C-F, Chen C-C, Tung L, et al (2002) The yeast ADP-ribosylation factor GAP, Gcs1p, is involved in maintenance of mitochondrial morphology. *J Cell Sci* 115:275–82.
128. Kawada D, Kobayashi H, Tomita T, et al (2015) The yeast Arf-GAP Glo3p is required for the endocytic recycling of cell surface proteins. *Biochim Biophys Acta* 1853:144–56. doi: 10.1016/j.bbamcr.2014.10.009
129. Agrawal G, Fassas SN, Xia Z-J, Subramani S (2016) Distinct requirements for intra-ER sorting and budding of peroxisomal membrane proteins from the ER. *J Cell Biol* 212:335–48. doi: 10.1083/jcb.201506141
130. Yonekawa S, Furuno A, Baba T, et al (2011) Sec16B is involved in the endoplasmic reticulum export of the peroxisomal membrane biogenesis factor peroxin 16 (Pex16) in mammalian cells. *Proc Natl Acad Sci U S A* 108:12746–51. doi: 10.1073/pnas.1103283108
131. van der Zand A, Braakman I, Tabak HF (2010) Peroxisomal membrane proteins insert into the endoplasmic reticulum. *Mol Biol Cell* 21:2057–65. doi: 10.1091/mbc.E10-02-0082
132. Heyman JA, Monosov E, Subramani S (1994) Role of the PAS1 gene of *Pichia pastoris* in peroxisome biogenesis. *J Cell Biol* 127:1259–73.
133. Erdmann R, Blobel G (1996) Identification of Pex13p a peroxisomal membrane receptor for the PTS1 recognition factor. *J Cell Biol* 135:111–21.
134. Warren DS, Morrell JC, Moser HW, et al (1998) Identification of PEX10, the Gene Defective in Complementation Group 7 of the Peroxisome-Biogenesis Disorders. *Am J Hum Genet* 63:347–359. doi: 10.1086/301963

135. Shimozawa N, Imamura A, Zhang Z, et al (1999) Defective PEX gene products correlate with the protein import, biochemical abnormalities, and phenotypic heterogeneity in peroxisome biogenesis disorders. *J Med Genet* 36:779–781.
136. Santos M, Imanaka T, Shio H, Lazarow P (1988) Peroxisomal integral membrane proteins in control and Zellweger fibroblasts. *J Biol Chem* 263:10502–10509.
137. Budzinski KL, Allen RW, Fujimoto BS, et al (2009) Large structural change in isolated synaptic vesicles upon loading with neurotransmitter. *Biophys J* 97:2577–84. doi: 10.1016/j.bpj.2009.08.032
138. Daniels RW, Collins CA, Chen K, et al (2006) A Single Vesicular Glutamate Transporter Is Sufficient to Fill a Synaptic Vesicle. *Neuron*. doi: 10.1016/j.neuron.2005.11.032

Curriculum Vitae

Personal Information

Name: Kareem Salah Ahmed Soliman

Nationality: Egyptian

Marital status: Married

Birthdate: October.27.1987

e-mail: kareemsoly@yahoo.com

Tel: +49 01575 1827286



Education

PhD in Molecular Medicine under the Direction of Prof. Jutta Gartner Lab. Pediatric Department - Medical Center University of Gottingen, Germany (Feb 2013-Present)

M.Sc. Degree in Neuroscience International Max Planck Research School – Thesis title “Cytomatrix Active Zone (CAZ) STED Nanoscopy” Research work was conducted under the Direction of Prof. Thomas Dresbach Lab, Gottingen Germany (2010-2012)

B.Sc. Pharmacy and Biotechnology, German University, Cairo (GUC) Egypt (2004-2009)

Work Experience

2013-Present: Wissenschaftler Mitarbeiter at the University Medical Center (UMG), University of Göttingen, Germany.

2010-2012: Master studies at the International Max Planck Research School of Neuroscience, Gottingen, Germany.

2009-2010: Teaching staff member in the department of Pharmacology and Toxicology, College of Pharmacy in Pharos University in Alexandria, Alexandria Egypt.

Teaching Experience

2011-2012: Postgraduate Method Course “Neuroanatomy and Development”, International Maxplanck Research School, Gottingen Germany

2009-2010: Undergraduate Pharmacy Courses, Faculty of Pharmacy and Drug Manufacturing, Pharos University in Cairo, Alexandria Egypt

2008-2009: Workshop “RNAi therapeutics”, Bibliotheca Alexandrina, Alexandria Egypt

2008-2009: Workshop “Complementary Medicine and Alternative Medicine”, Bibliotheca Alexandrina, Alexandria Egypt

Scholarships and Awards

Max Planck Society (MPI) Scholarship - Germany (2010-2011)

Professional licenses

Pharmacy Practice license, Egypt.

Memberships

Genetic Society of America (GSA) since 2015

Publication Record

Peer-Reviewed Journals (hyperlinks are active)

1. **Kareem Soliman** “CellProfiler: Novel Automated Image Segmentation Procedure for Super-Resolution Microscopy” *Biological Procedures Online* BMC 201517:11 DOI: 10.1186/s12575-015-0023-9

2. Yifat Cohen, Yoel Alexander Klug, Lazar Dimitrov, Zohar Erez, Silvia G. Chuartzman, Dalia Elinger, Ido Yofe, **Kareem Soliman**, Jutta Gärtner, Sven Thoms, Randy Schekman, Yael Elbaz-Alon,* Einat Zalckvar* and Maya Schuldiner* "Peroxisome Juxtaposed" *Mol. BioSystems* RSC, 2014, **10**, 1742-1748 **DOI:** 10.1039/C4MB00001C

Conference Posters

1. **K. Soliman** "Novel Automated Imaging Segmentation Procedure for Super Resolution Imaging" Seeing is Believing EMBL meeting, Heidelberg Germany (2015)
2. Maria Bartel M.Sc., Hao Guo, **Kareem Soliman**, Dr. Tobias Schleuß Fast and effective characterization of Ultrafiltration membranes. International Congress on Membranes and Membrane Processes ICOM, Amsterdam Netherlands (2011).

Matlab codes (hyperlinks are active)

1. **Kareem Soliman** "FWHM automated script". Calculates signal FWHM from Gaussian fit for infinite number of .CSV data" (2016).

Computer skills

Microsoft word, PowerPoint and excel.

Lab. Skills and data analysis skills

Lab skills

1. Hippocampal and cortical cell culture preparation from mice.
2. Cell Culture, cloning and whole cell patch clamp.
3. Immunocytochemistry (ICC).
4. Super resolution microscopy (STED microscopy).
5. Yeast *saccharomyces cerevisiae* genomic integration and yeast super resolution imaging (nanobody labeling).

6. Protein western blot and Immunoprecipitation techniques.
7. Live cell super resolution imaging.

Data analysis

1. ImageJ imaging analysis software (NIH)
2. CellProfiler and CPA (www.cellprofiler.org)
3. Matlab Scripts (www.mathwork.com)
4. R-statistics and OriginPro statistics software.

Language

Arabic (Mother Language)

English (Proficient)

German (Very Good)

Scientific Lab Rotations

1. "Fiber Stimulation Patch clamp using Calyx of Held in mice brain slices to study molecular mechanisms of synaptic transmission" Department of Molecular Synaptic Transmission- Max Planck Florida, Palm Beach FL, USA. (October-January 2011/12)
2. "Fluorescence Correlation Spectroscopy using **STED** microscopy in Neuron Brain Slices" AG Stefan Hell, Max Planck Biophysical Institute, Göttingen Germany. (May-June 2011)
3. "Cut-Off determination of UF-membranes using aqueous mixtures of distinct molecules; new method" –AG Dr. Schleuss - Sartorius Stedim – Göttingen, Germany. (March-April 2011)
4. "Investigating the role of Synaptotagmin-3 in hippocampal neurons using imaging & electrophysiological techniques" –AG Dr. Camin Dean- European Neuroscience Institute (ENI) - Göttingen, Germany. (January-February 2011)
5. Testing a de novo approach which may evaluate cell viability via spectroscopic technique. Evaluating the neuron protection activity of **Fluoxetine** against alcohol toxicity–AG Prof. Kornhuber – Molecular

- Neurobiologie Lab – Psychiatry Klinikum - Erlangen University, Germany. (August-October 2008)
6. ASM gene (Acid Sphingomyelinase) different splice variants expression in MDD patients versus healthy volunteers" – AG Prof. Kornhuber – Molecular Neurobiologie Lab – Psychiatry Klinikum – Erlangen University, Germany. (July-October 2008).
 7. "Cloning ROS and NOS sensor" AG Prof. Richard Whorton. Department of Pharmacology. Duke University, Medical Center (Sep-October, 2007)

Professional development courses

1. Public Speaking Skills. Toastmasters International Club, (Scripps Institute) Palm Beach FL, USA
2. Certified attendance: "Introduction to Complementary and Alternative Medicine" e-learning course. (NIH).
3. Certified attendance: "Preventative Environmental Strategies" e-learning course (Lund University), Sweden.
4. Certified attendance: "Youth Leadership training course" (Cambridge University), England.

Conferences and events organizing Experiences

1. Molecular Medicine PhD Retreat in Wernigrode Germany (2015).
2. Computer Science Java Programming Workshop. Bibliotheca Alexandrina Egypt (2005).
3. 3rd Global Environmental Youth Convention (2004).

Conference participation

1. EMBL meeting: 'Seeing is Believing" Heidelberg, Germany (2015).
2. Molecular Medicine Program Retreat Wernigrode (2015).

3. Focus on Microscopy (FOM15), Gottingen Germany (2015).
4. Horizon meeting, Gottingen, Germany (2010).

Sport achievements (Fencing)

1. 3rd Place (**BRONZ Medal**) in the Egyptian National Schools Championship (2002).
2. 5th Place in the Egyptian National Tournament under 17 (FEA) (2003).
3. 1st, 2nd and 3rd (**GOLD, SILVER and BRONZ medals**) in the Egyptian Teams Tournament (2003/2004).